



**Politecnico
di Torino**

POLITECNICO DI TORINO

Master Degree course in Sustainable Nuclear Energy

Master Degree Thesis

Multiphysics analysis of ARC blanket

Supervisors

Prof. Sandra DULLA

Dr. Antonio FROIO

Dr. Alex AIMETTA

Dr. Nicolò ABRATE

Candidate

Marco CARAVELLO s270423

ACADEMIC YEAR 2021-2022

Acknowledgements

As I come to the end of this journey, I feel I am indebted to those who have accompanied me and helped allow me to get here.

I would especially like to thank Professor Sandra Dulla, Professor Antonio Froio, Dr. Alex Aimetta and Dr. Nicolò Abrate for helping me with my thesis work, showing me, once again, their best side, always ready to support me and make me feel part of a great team. Thank you very much indeed.

A special mention goes to Dr. Giuseppe Francesco Nallo, without whom I probably would not have made so many of the choices I have made in past years. He deserves credit for showing me what it means to put passion into own work and for introducing me to the world of OpenFOAM.

Thanks to the colleagues and colleagues who have become friends, whom I met during the years at the Polytechnic, without you these years would not have been as intense and stimulating.

Thanks to my lifelong friends whom I know I can always count on.

Thanks to my family for having supported me, in all respects, from the very first day of my arrival in Turin. Without you, none of this would have been possible.

With this job an important part of my life comes to an end, let us see what happens next!

Abstract

The Affordable Robust Compact (ARC) reactor is a conceptual design of a nuclear fusion reactor developed by MIT Plasma Science and Fusion Center; its main objective is to demonstrate the feasibility and the advantages of compact high magnetic fields - produced by REBCO high temperature superconducting tapes in demountable coils - and of inboard radio frequency lower hybrid current drive launchers, ensuring a steady state condition for plasma and the consequent power generation. ARC includes a fully liquid blanket consisting of FLiBe, i.e. a molten salt made by a 2:1 LiF-BeF₂ mixture, serving, simultaneously, as tritium breeder, neutron multiplier, heat-transfer fluid and neutron shielding material. The design foresees a high efficiency Brayton cycle to extract heat from high temperature FLiBe (around 900 K) and produce electricity.

With the aim of performing a multi-physics analysis of the Breeding Blanket (BB), a coupling procedure between two finite volume tools has been developed. To this aim, the *nemoFoam* package has been written. This code includes a solver for the multi-group diffusion equation, with the purpose of modelling the 3D neutronic behaviour of a given system and the official thermal-hydraulic *OpenFOAM* solver for conjugate heat transfer problem in multiple regions, which has been slightly modified for the purposes of this work. Both codes are written in the *OpenFOAM* environment, a free open source framework for developing executable applications. Being the physical phenomena involved strongly interdependent, performing a multi-physics analysis is the natural choice to resolve properly the effects of such physical interplay connection.

Exploiting this in-house tool, this analysis presents the power field deposited by neutrons, the steady state flow and temperature fields of the FLiBe inside the blanket tank, under nominal operating condition, as well as the temperature distribution across the solid layers between the plasma chamber and the BB.

Contents

1	Introduction	1
1.1	The ARC reactor	2
1.2	Aim of the work	3
2	System model	5
2.1	Design of the ARC reactor	5
2.2	Neutronic modelling	10
2.3	Thermal-hydraulic modelling	15
2.4	Finite volume modelling	19
2.4.1	Finite Volumes and OpenFOAM	20
3	nemoFoam benchmark	23
3.1	Benchmark setup	24
3.2	Benchmark results	27
4	Simulation workflow	33
4.1	CAD production	33
4.2	Meshing	35
4.3	Neutronic setup	37
4.4	Thermalhydraulic setup	39
4.5	Results	43
4.5.1	Power Deposition	43
4.5.2	Flow field	44
4.5.3	Temperature map	49
4.5.4	Pressure field	52
5	Conclusion	53
	Bibliography	55

Chapter 1

Introduction

One of the major challenges that our society is called to face nowadays is reducing the carbon footprint of the whole human activities. Electricity generation accounts for more than the 40% of total energy related CO₂ emissions in the atmosphere [1]. In view of the continuous electrification, the global electricity demand is expected to grow [2] and the correlated production cannot be farther based on fossil fuels. Therefore, alternative power sources are envisaged to increase their shares in the energy mix and take place of the traditional, carbon-based ones. Nuclear power can hold an increasingly important role in the so-called energy transition. Today fission plants represent a worldwide, secure, reliable and safe electricity generation technology [3], nevertheless nuclear fusion is considered to be the promising future disruptive innovation in the nuclear energy field [4].

Current fusion reactor designs feature as fuel a uniform mixture of hydrogen isotopes (Deuterium and Tritium), which, under extreme pressure and temperature conditions, produce nuclear fusion reactions. Deuterium is quite common in nature because is present in seawater with a ratio of 1 deuterium atom (D) for about 7000 atoms of hydrogen (H), allowing to be physically separated at a competitive cost. Tritium (T), instead, is radioactive, with a half-life of a bit more of 12 years [5], making it impossible to find on Earth. However, it can be obtained from interactions between neutrons and Lithium isotopes (breeding reactions): Li⁶ produce an exothermic reaction, contrary to Li⁷ which requires energetic neutrons to produce T atoms.

Initiating fusion reaction thresholds can be reached, on Earth, in specific, complex machines, where the gas mixture, brought to the state of plasma, must be kept confined by means of one of several techniques. Multiple reactor designs are studied worldwide, but the most common, at least in Europe (in reactors like DEMO, ITER, JET), are the tokamaks, in which plasma confinement is achieved by using magnetic fields produced by superconducting magnets and therefore is called "magnetic confinement". Once the requirements for fusion are reached, those reactions take place inside the plasma producing a nucleus of He⁴ (also called alpha particle) and a neutron per reaction. Being the Helium-4 a stable particle, the only radioactive potentially harmful side effect of fusion reactions products is the activation of the materials (produced by neutrons) that surround plasma. Unluckily, the reaction in analysis require the use, as part of fuel mix, of a radioactive gas (T) with a relatively short life that must be artificially produced. Up to now, the

best solution to accomplish the tritium issue is to breed Lithium, using fusion generated neutrons, in dedicated region of the reactor that surrounds the plasma chamber, called Breeding Blanket (BB). It is inside the BB that the high energy neutrons, coming from the plasma, will deposit the largest amount of power, making it the most critical component for what regards the heat extraction system and the Balance Of Plant [6].

1.1 The ARC reactor

The Affordable Robust Compact (ARC) is the design of a fusion reactor currently under development at Commonwealth Fusion Systems which is a spin-off of the Massachusetts Institute of Technology's Plasma Science and Fusion Center. It has been projected to be a breakthrough in the path towards nuclear fusion power plants, aiming to serve as testing environment as well as demonstration pilot plant [7].

ARC, as name could suggest, is a compact machine with smaller dimensions with respect to other nuclear fusion designs such as DEMO [8] and ARIES [9]; the small size has an impact on the thermal power produced, targeting a related electrical output of 200-250 MWe, about 5 times smaller than the classical power output of the reactors previously mentioned. Having smaller reactor dimensions makes the magnets closer to the plasma, producing higher magnetic fields, recalling the inverse proportionality dependency of the magnetic field and the distance from the coil, allowing better plasma control and performances [7]. The advantages of having reduced power output and dimensions are also economic based and related to the reduction of both the capital cost investment and the risk of failures.

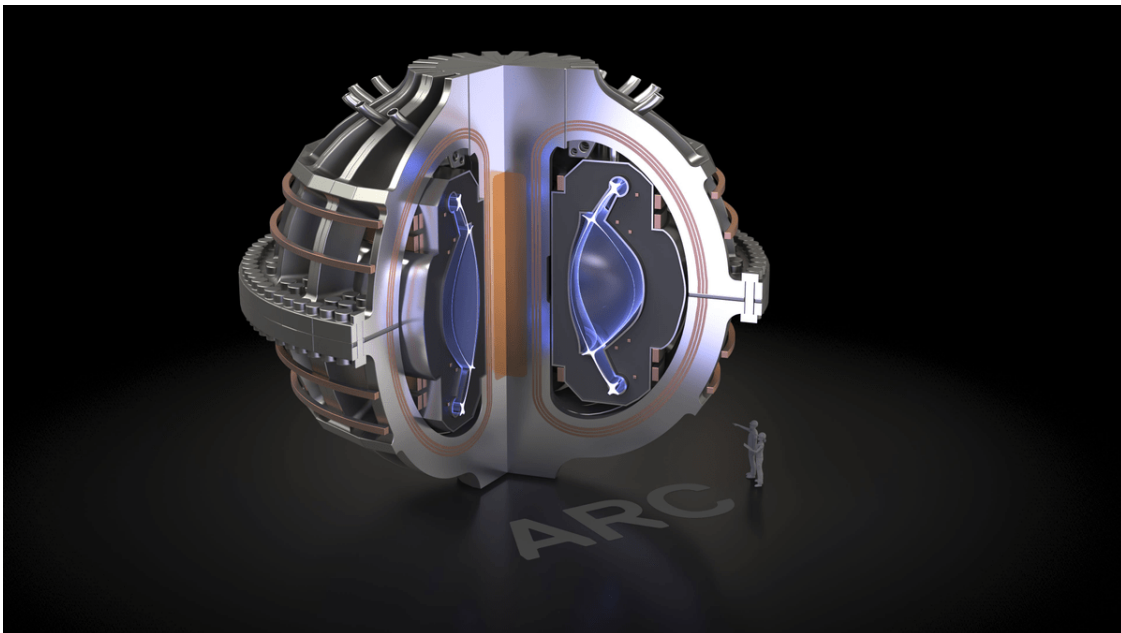


Figure 1.1: ARC concept design [<https://cfs.energy/technology/arc-commercialization>] [12].

The plasma (50% D - 50% T) is magnetically confined by means of high magnetic fields (with a peak of more than 20 T on coils) produced by REBCO (Rare-Earth Barium Copper Oxide) superconducting toroidal field coils which are High Temperature Superconductors (HTS) that can operate up to around 80 K, but are however maintained at a temperature of 20 K [10]. This choice permits to use as coolant not only the liquid Helium, but also gaseous Helium, liquid Neon and liquid Hydrogen, with the latter preferred respect to the others due to the abundance and the low cost. The nominal temperature of magnets operations, above the 4.2 K usually required for Low Temperature Superconductors [10], exploits the materials ability to absorb heat without losing superconductivity since their heat capacity at 20 K is much higher than at 4.2 K. Moreover, HTS permit to use resistive joints in coils so that they can be manufactured as demountable, making possible modular maintenance and fast the substitution of the vacuum vessel.

The introduction of innovative inboard radiofrequency launchers allows to provide a non-inductive current drive with the effect of producing a stable plasma, overcoming the limiting issue of pulsed power production due to the way (transformer principle) in which plasma current is usually obtained [11].

The blanket of ARC consists of a tank filled with a molten salt (FLiBe) that holds four different key functions: moderating the 14.1 MeV neutrons produced inside the plasma to breed the Lithium present into the salt and produce Tritium; increasing the number of neutrons thanks to the interactions of the neutrons generated in the plasma with the Beryllium nuclei; extracting the heat deposited by neutrons in the solid materials in the inner shells of the reactor ensuring that the maximum allowed temperatures are never overcome and, together with the fraction of heat deposited directly into the fluid, export it to the Balance Of Plant; shielding the external equipment from neutron radiation. To accomplish the tasks FLiBe is constantly injected at a temperature of 800 K, such that it is far enough from its freezing point (732 K) [13].

1.2 Aim of the work

As in classical thermal power plants, many aspects must be considered to design appropriately the heat extraction system in order to ensure that thermal limits are not overcome. In a fusion reactor additional complexity is introduced because of the nature of the heat source and of the mechanisms of power deposition in the materials surrounding the plasma. The discontinuities of power deposition values in adjacent layers make necessary to model the heat source term as better as possible. This is because the nuclear properties of materials depend both on temperature of the material and on the energy of the interacting neutrons.

This thesis is focused on the multiphysics analysis of the ARC reactor Blanket, where, with multiphysics, it is intended a neutronic and thermal-hydraulics analyses, since the thermal-mechanical part of the problem is not addressed. The study is carried out in OpenFOAM, a finite volume open source framework for developing executable applications [14]. It is well established in the field of Computational Fluid Dynamics [15], but its flexibility makes it suitable to perform analysis that are not strictly related with thermalhydraulics, as in the case of the nemoFoam neutron diffusion code developed for this

thesis. The main objectives addressed in this work are the computation for each region of the power deposition field and of the temperature distribution, and for the fluid domains the flow and the pressure field, because those fields have a strong influence on the Balance Of Plant, whose ultimate scope is to generate electricity with the highest efficiency.

In chapter 2 the design of ARC used in this work is presented and the physical modelling of the problem is addressed.

The benchmark of the developed neutronic tool is presented in chapter 3.

Chapter 4, following the simulation workflow, presents the rationale behind the choices that have been taken to produce the CAD files, the meshes and the case setups. Finally, the results are reported in section 4.5.

Chapter 2

System model

2.1 Design of the ARC reactor

ARC is an innovative design of nuclear fusion reactor, which makes compactness, reduction of required material volumes, capital investments and flexibility its strengths. Having smaller dimensions allows to minimise the space occupation by accurately selecting the component materials in order to get overall performances compliant with the objectives that ARC aims to achieve. The comparison with ITER, a comparable power output machine, and JET, a comparable machine in size, gives the idea of the its exceptional attractive features.

Reactor	Major Radius	Minor radius	Plasma Volume	Plasma Power	Q
ARC [7]	3.3 m	1.1 m	141 m ³	525 MW	13.5
ITER [16]	6.2 m	2.0 m	830 m ³	500 MW	10
JET [17]	2.96 m	1.25 m	100 m ³	-	-

Table 2.1: Comparison of tokamak characteristics.

In table 2.1, the last column reports the so called fusion energy gain factor, indicated with the letter Q, defined as the ratio between the power produced in the plasma from fusion reactions and the power needed to keep the plasma in fusion compliant conditions. It must be pointed out that JET, which started the operations in 1983, "was designed to study fusion in conditions approaching those needed for a power plant" [18], but it did not have, at that time, the goal of sustaining a steady core plasma, so it makes no sense to define a plasma power and a power gain for it.

As it is possible to see from the figure 2.1, ARC blanket is made up of several different components, each one with different tasks. In order, from the plasma side to the external world, the first component is the 1 millimeter thick First Wall made of tungsten (FW). The choice of the FW material is fundamental in view of Tritium Breeding Ratio (TBR) evaluation, being this parameter very sensitive on the combination of FW thickness and composition. [7] The TBR corresponds to the ratio of the Tritium burning rate in the plasma chamber and the rate of its production inside the blanket. Over the years there

has been a refinement in the designated FW thickness since it was originally set to 1 cm, with the effect of producing a small amplification of the TBR value as shown in [22] where it is found that the thinner the FW the closer the TBR to 1.05 despite of the selected first wall material. Moreover, the tungsten choice is compliant with the issues of disruptions (consisting in a rapid and uncontrollable power release due to the loss of plasma confinement), during which the Plasma Facing Components (PFC), receive large amount of power and heat up very violently. The violent increase in temperature could bring to the partial melting of the FW modules, which would deform and require a substitution; on its side, the melting point of the tungsten is very high (over 3700 K), providing a wide temperature gap before actual occurrence of the melting.

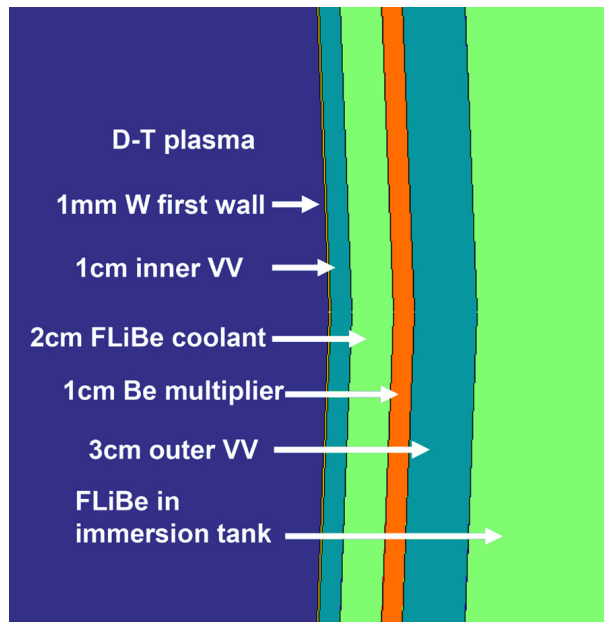


Figure 2.1: Scheme of the blanket layers [22].

The double wall Vacuum Vessel (VV), in the current design, is made of Inconel718, a corrosion compliant Nickel-Chromium alloy [39]. In the future, it could be substituted by a different material because, despite of good corrosion resistance and high strength at high temperatures, the presence of Nickel is an issue from the nuclear activation point of view. The VV design exploits the possibility, offered by the combination of a liquid blanket and the demountability of coils, of manufacturing and testing components as single pieces, producing a reduction of the installation time. The Vacuum Vessel being subjected to thermo-mechanical stresses, neutron irradiation related damage and FLiBe corrosion, is expected to be substituted throughout the reactor life.

The neutron multiplier (NM) 1 cm thick Beryllium layer, is attached to the outer VV, without any structural purposes. Its main goal is to increase the number of neutrons able to breed the Lithium present in the blanket tank, contributing to raise the TBR above the unity [7]. Actually, some studies show that, with a similar configuration and under nominal condition, ARC is able to reach a TBR higher than 1.1, producing a positive

margin to compensate non perfect Tritium extraction and possible leakages, not only ensuring the self-sufficiency of the single plant, but also producing a reservoir for the start up of other reactors.

Between the Vacuum Vessel cavity, FLiBe flows, in a complex circuit characterized by many inlets and outlets. According to fig. 2.2 the coolant is injected in the coolant channel from four different inlets and is expected to enter the blanket tank from three connection ports.

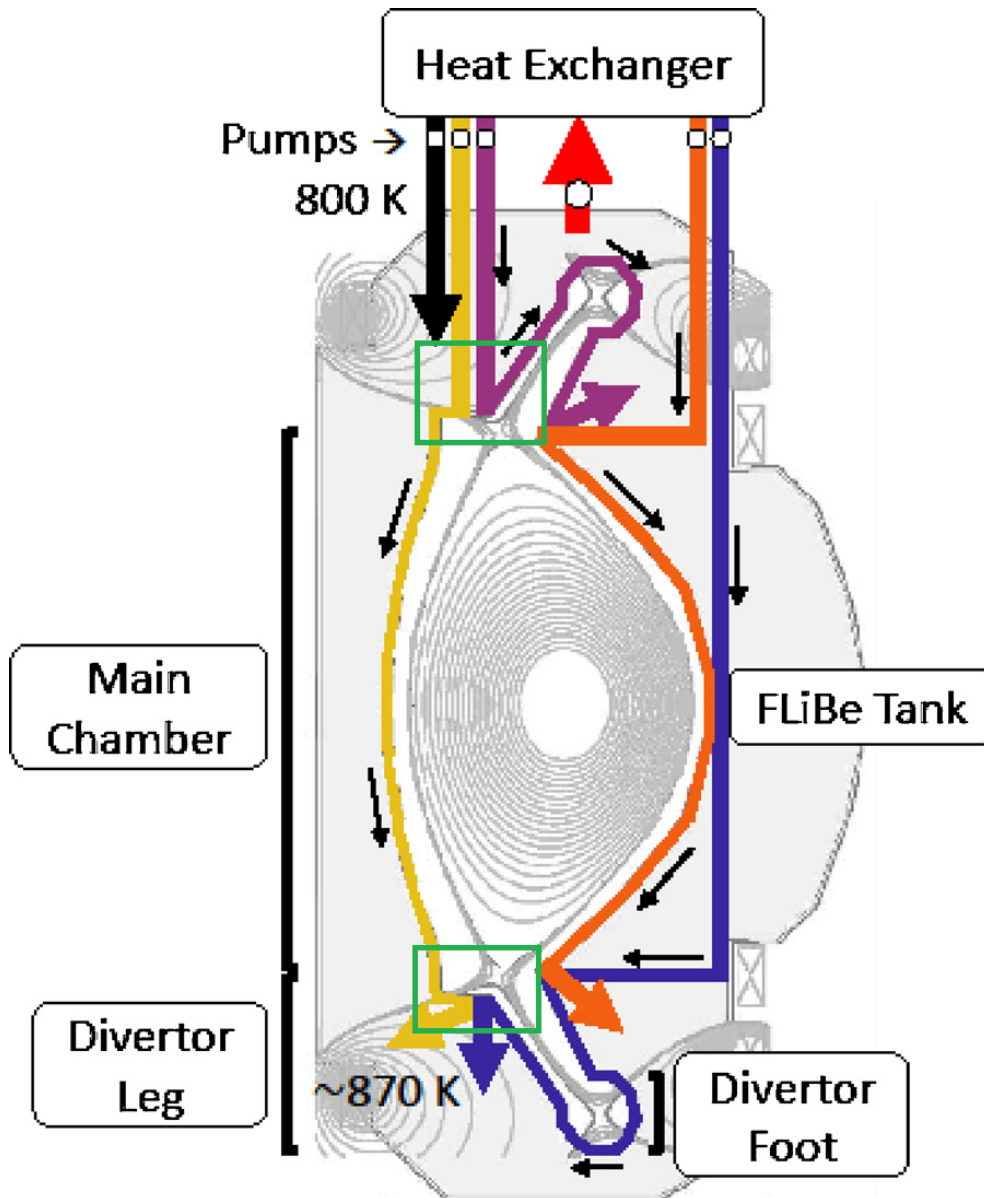


Figure 2.2: Scheme of the hydraulic layout of the blanket [22].

Each color represents a different path, it is important to underline that each path aims

to cool a different section of the reactor: purple and violet paths focus on the cooling of the divertors, while yellow and orange on the inner and the outer side of the structure. The black path is the only exception, consisting in stream of FLiBe directly injected into the tank, to help cooling the region where it is expected to have higher temperatures. The coolant, ultimately, exits from the tank through pipe located at top of the blanket and reaches the heat exchanger where will it heat up the operating fluid of the secondary circuit, that will produce electricity in a Brayton cycle.

The advantage of having such a complex flow path is the capability of extracting additional power that could be deposited in the components during transients without changing the total FLiBe flow rate: the coolant usually sent directly to the tank (through the black path) can be diverted to the coolant channel if needed.

In this work a simplified configuration is taken as reference: the FLiBe enters in the coolant channel only from the yellow path port, reaches the tank from the purple port (highlighted by green boxes in figure) and leaves the tank from the usual outlet pipe. This choice is coherent with the design analyzed in [21], obtained by the authors after an interaction with the ARC designers.

Even if ARC design foresees divertor plates rather than a limiter, no configuration was investigated until 2018 [22]. Divertors are fundamental to maintain fusion favourable conditions inside plasma, by extracting reaction products (alpha particles) and other possible impurities. In magnetically confined plasmas, many concentric closed poloidal flux surfaces develop: the first region, in radial direction, outside of the last closed surface is called Scrape-Off Layer (SOL) and it is where charged energetic particles, which left the plasma, start moving along the open magnetic flux surfaces specifically generated, towards the divertor targets. Such open surfaces are produced by means of additional poloidal field coils which produce a magnetic poloidal field that, interacting with the field generated by the plasma current, resulting in a null poloidal field point, called X-point. In [21] Kuang et al. propose not a single, but a double-null X-point target configuration, more complex but able to sustain higher heat fluxes. The power carried by charged particles is in the order of one fifth of the total plasma power [5], plus the power used to heat the plasma by means of radio-frequency, for a total of about 150 MW, around 35% of it is expected to radiate, therefore about 100 MW enter in the SOL and reach, equally partitioned, the divertor targets. The total surface area of the targets is 66 m², producing an average heat flux of 1.5 MW/m² [22]. The arrangement selected for the divertor heat exhaust management, consist in swirl tubes of 12 mm diameter in which FLiBe flows at 2 m/s, passing housed within the tungsten first wall.

As it is possible to see from fig. 2.3 the composition of layers is very different from the ones presented in fig. 2.1, however keeping in mind that the aim of the work is to perform a multiphysics analysis of the blanket, it has been chosen to treat the divertor regions as common regions. The effect of such simplification is expected to be not dramatic, being the neutronic fluxes expected to be 2 orders of magnitude lower than in the plasma facing regions [20].

As previously reported, the nominal plasma power of ARC is 525 MW, of which 420 MW (corresponding to the 80% of the total) are carried by the neutrons outside of the plasma, however, it has been shown that additional power sources exist because

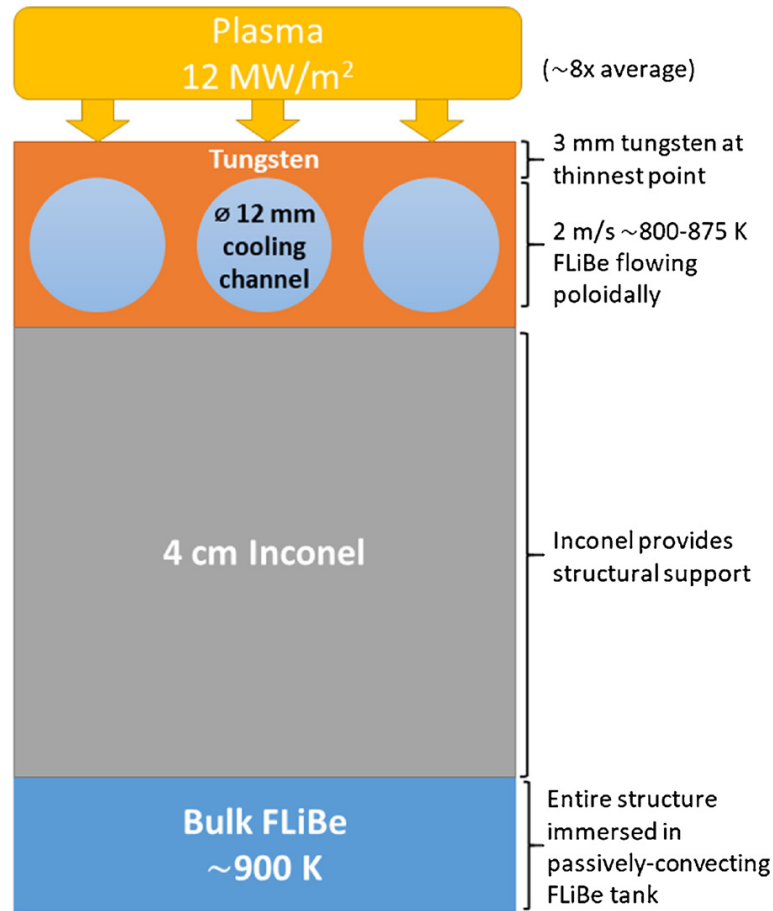


Figure 2.3: Cross section of the layer structure in the divertors [22].

of the comprehensive mechanism of power deposition is much more complex [22]. The total amount of power deposited in the Blanket is higher than the expected, due to the breeding reactions that occur in the BB (FLiBe is 90% enriched in Li^6 which produce exothermic reactions). Also photons, produced by neutrons, after interactions with the reactor materials, play an important role in power deposition, in particular for Tungsten and Inconel718 [20]. Fixed the amount of thermal power produced in plasma, different operational phase were been defined in [22], identifying a Fusion Nuclear Science Facility (FNSF) phase, a Pilot phase with conservative conditions and a very aggressive one. Each phase is characterized by different inlet velocities of FLiBe: the advantages of reducing the flow rate consist in an increase of output temperature of FLiBe, with a subsequent more efficient Brayton cycle (the aggressive phase would bring to a thermal efficiency of 0.5 obtained with an outlet temperature of the FLiBe of 1200 K). The more efficient the thermodynamic cycle, the more power transferred to the secondary circuit and the more electricity generated. Moreover, having reduced flow rates would also contribute to the reduction of the corrosion caused by the FLiBe, mainly in the coolant channel (where the flow area is small and the velocity increases). In [22] the improved forced flow circuit of

fig 2.2 has been introduced, foreseeing a input flow velocity of FLiBe of 2 m/s in order to match a temperature increase in the coolant channel of 75 K. According to the carried analysis the maximum temperature of FLiBe would be about 910 K, compliant with the 1000 K Inconel718 maximum operating temperature.

2.2 Neutronic modelling

Predicting the distribution of neutrons in the space, energy and time corresponds to the aim of the neutron transport theory. Indeed, neutron propagation in media is a complex phenomenon governed by the so called Boltzmann equation for neutrons, which models the interactions of the neutral particles with the nuclei constituting the matter.

Many types of interaction can occur, all of them are represented by a set of interaction parameters, called cross section (Σ), dependent on the materials and on the energy of neutrons.

Unluckily, deriving the equation is easier than solving it. For this reason two branches developed during the years to provide solutions of the neutron transport equation: probabilistic and deterministic methods.

The former are based on Monte Carlo (MC) methods which simulate, repeatedly, randomness governed experiments inside a given system and collect the outcomes. At the end of the numerical procedure, MC methods will produce a set of expected values of the variables under examination. The more experiments are performed, the more accurate (i.e. with lower statistical uncertainty) the results will be. It is a very powerful method, because it allows to solve the exact neutron transport equation also in very complex geometries. Its main drawback is the huge amount of computational power required, since its convergence rate is $N^{0.5}$, where N is the number of simulated experiments.

Deterministic methods, on the other side, provide solutions for slightly simplified versions of the Boltzmann neutron transport equation. Here, there is probably the main difference between the two branches: MC methods produce a solution of the exact problem without actually "solving" the equation in the more traditional sense, the deterministic approaches solve not the exact problem, but a physically distorted one. Physical distortion can occur in the energy treatment of the problem because of a grouping process; in the direction of neutron flight by allowing only some certain directions, and so on. The principal deterministic methods developed since the dawn of nuclear engineering are the Method of Discrete Ordinates, the Method of Spherical Harmonics and the Diffusion theory (with the possible multi-group upgrade). In this work the neutrons propagation inside the ARC reactor is studied by means of the multi-group diffusion theory.

In fact, under some specific hypothesis the transport equation can be extensively simplified, and even if all the diffusion requirements are not fully respected, the provided solution represents a good approximation of the correct one [23]. Neutrons can be considered as point particles, meaning that the position \vec{r} and the velocity \vec{v} can describe completely their distribution in a domain called "phase space". The velocity vector [24] can be rewritten as:

$$\vec{v} = v\vec{\Omega}, \tag{2.1}$$

where v is the magnitude of the velocity of the neutron (knowing its energy and mass can also be computed as $v = \sqrt{2E/m_N}$) and $\vec{\Omega}$ is the unit vector in the direction of its motion.

Introducing, at this point, the neutron angular density function $n(\vec{r}, E, \vec{\Omega}, t)$ as the probable number of neutrons present at position \vec{r} , per unit energy E and per unit direction $\vec{\Omega}$ at time t , it is possible to integrate over the solid angle, in order to consider all the possible directions in which neutrons can travel, leading to the neutron density:

$$n(\vec{r}, E, t) = \int_{4\pi} n(\vec{r}, E, \vec{\Omega}, t) d\Omega. \quad (2.2)$$

Following an analogous procedure, it is possible to define a new quantity, called the vector flux (or angular current):

$$\vec{\phi}(\vec{r}, E, \vec{\Omega}, t) = n(\vec{r}, E, \vec{\Omega}, t) \vec{v}. \quad (2.3)$$

Its magnitude, the scalar flux, when is integrated over the solid angle, gives the total flux, that is the quantity mainly used in this work, and will be usually referred as "flux":

$$\Phi(\vec{r}, E, t) = \int_{4\pi} n(\vec{r}, E, \vec{\Omega}, t) v d\Omega. \quad (2.4)$$

It is very important to understand that the quantity $\Phi(\vec{r}, E, t)$ is not representative of the neutron flow (in the sense of quantifying the neutrons moving across any surface), rather it is a measure of the overall motions governed by collision phenomena. Lamarsh, given the proportionality of the flux to $n(\vec{r}, E, t)$, suggests to consider it on a par with chemical concentration or density of atoms [23].

The quantity that gives information of the flow of neutrons, instead, is called neutron current density vector and is denoted by $\vec{J}(\vec{r}, E, \vec{\Omega}, t)$.

Defining a surface area dA and its normal \hat{n} , it is possible to compute the net number (counted positive if neutrons move in the direction of \hat{n} , negative otherwise) of neutrons crossing that surface per unit energy, per unit solid angle, per unit time:

$$\#(\text{net}) \text{ Neutrons crossing } d\vec{A} = \int_{4\pi} dA \hat{n} \cdot \vec{\phi}(\vec{r}, E, \vec{\Omega}, t) d\Omega = dA \hat{n} \cdot \int_{4\pi} \vec{\phi}(\vec{r}, E, \vec{\Omega}, t) d\Omega, \quad (2.5)$$

where the last integral is the actual definition of $\vec{J}(\vec{r}, E, \vec{\Omega}, t)$, which is a vector having as components the net number of neutrons crossing the unit area surfaces with normal parallel to the directions pointed by the versors of the components.

Having defined the necessary variables for the treatment of the problem, it is possible to proceed further to develop a continuity equation for neutrons. In a non-multiplying medium (which is the case of a fusion reactor) where all the neutrons are assumed to have the same energy (this assumption will be released later) and focusing on the total density, let's consider a packet of neutrons $n(\vec{r}, t) d\vec{r}$, as they move in a time interval dt . Some of them will suffer a collision (and will be lost from the group because of the interaction phenomena with the nuclei) and new "external" neutrons could join the packet thanks the injection of an external source. Of the initial group, only the neutrons that did not

suffer any interaction will remain in the packet. Quantifying the probability of having an interaction by means of $\Sigma v dt$ (i.e. the probability of having an interaction per unit path times the travelled distance in dt), it is possible to compute the surviving neutrons as:

$$\#Remaining\ neutrons = (1 - \Sigma v dt) n(\vec{r}, t) d\vec{r}. \quad (2.6)$$

Given the source injection rate $S(\vec{r}, t)$, it is possible to compute the number of neutrons introduced in the system by the source as:

$$\#Source\ injected\ neutrons = S(\vec{r}, t) d\vec{r} dt. \quad (2.7)$$

Summing up the terms, it is possible to define the number of neutrons in the packet at position $(\vec{r} + d\vec{r})$ and time $(t+dt)$ as:

$$n(\vec{r} + d\vec{r}, t + dt) d\vec{r} = (1 - \Sigma v dt) n(\vec{r}, t) d\vec{r} + S(\vec{r}, t) d\vec{r} dt, \quad (2.8)$$

rearranging the terms, the result is:

$$\frac{n(\vec{r} + d\vec{r}, t + dt) - n(\vec{r}, t)}{dt} = -\Sigma v n(\vec{r}, t) + S(\vec{r}, t). \quad (2.9)$$

The left hand side of the previous equation is nothing but the total derivative of $n(\vec{r}, t)$, where $(\vec{r} + d\vec{r}) = \vec{r} + \vec{v} dt$:

$$\frac{\partial n(\vec{r}, t)}{\partial t} + \nabla \cdot (n(\vec{r}, t) \vec{v}) = -\Sigma v n(\vec{r}, t) + S(\vec{r}, t), \quad (2.10)$$

and, rewriting in terms of neutron current and total flux:

$$\frac{1}{v} \frac{\partial \Phi(\vec{r}, t)}{\partial t} + \nabla \cdot (\vec{J}(\vec{r}, t)) = -\Sigma \Phi(\vec{r}, t) + S(\vec{r}, t). \quad (2.11)$$

Equation 2.11 is the continuity equation for neutrons, in which the time derivative represents the time rate of change of the neutron density, while the divergence term represents the change of $n(\vec{r}, t)$ associated to streaming. It is an exact equation for the medium previously defined (non multiplicative, with mono-energetic neutrons).

Under the following assumptions, it is possible to obtain a relationship between current and flux in order to produce a simplified solution [23]:

1. Infinite medium;
2. Uniform medium;
3. Absence of source inside the medium;
4. Isotropic scattering;
5. Slowly varying flux with respect to position;
6. Time independent problem.

The relationship turns out to have the same form of the Fick's law, meaning that the neutrons moves, i.e. create a current, from the regions of high densities (i.e. high values of flux) to regions of low densities: the magnitude of the current is proportional to the gradient of the flux, where the proportionality constant, indicated by letter D , is called diffusion coefficient.

$$\vec{J} = -D\vec{\nabla}\Phi, \quad (2.12)$$

D depends on the properties of the diffusive medium and in particular can be computed as:

$$D = \frac{\Sigma_{scattering}}{3\Sigma_{transport}^2}. \quad (2.13)$$

Inserting equation 2.12 in equation 2.11, it is possible to retrieve an equation for the total flux, the so called neutron diffusion equation:

$$\frac{1}{v} \frac{\partial\Phi(\vec{r}, t)}{\partial t} - \nabla \cdot (D\vec{\nabla}\Phi(\vec{r}, t)) = -\Sigma \Phi(\vec{r}, t) + S(\vec{r}, t). \quad (2.14)$$

Relaxing the initial assumption of monoenergetic neutrons, an additional phenomenon should be taken into account: the energy exchange between neutrons and nuclei during scattering interactions. Imagine of having defined multiple neutrons packets, for example two, one for neutrons with energy lower than a certain threshold E_0 (packet 0) and one for the more energetic neutrons (packet 1). While diffusing, neutrons, in principle, can receive and give energy from the surrounding environment. This possibility allows neutrons of packet 1 to leave the original packet and appear, after a collision, in the packet 0, or viceversa (even if it is less probable). Equation 2.14 must be slightly modified to take into account this new phenomenon:

$$\frac{1}{v_i} \frac{\partial\Phi_i(\vec{r}, t)}{\partial t} - \nabla \cdot (D_i\vec{\nabla}\Phi_i(\vec{r}, t)) = -\Sigma_i^{abs} \Phi_i(\vec{r}, t) + \sum_{j=1}^{N, i \neq j} (\Sigma_{j \rightarrow i}^{scat} \Phi_j) - \sum_{j=1}^{N, i \neq j} (\Sigma_{i \rightarrow j}^{scat} \Phi_i) + S_i(\vec{r}, t). \quad (2.15)$$

(for $i = 1, \dots, N$)

In this way, the first sum computes the neutrons that appear in the i -th group because of scattering from other groups and the second term for disappearing neutrons from group i . Equation 2.15 is the multi-group diffusion equation for non multiplying media. In order to solve it and since it is a partial differential equation, some boundary and initial conditions are needed. Initial conditions consist, trivially, in information on the initial states of the system. Boundary conditions (BC) require more attention.

If the boundary is a so called "free surface", i.e. a surface of a dense medium in contact with a very rarefied one (such that the external medium can be treated as vacuum), no neutron is expected to enter from vacuum inside the reactor.

For these cases a mixed boundary condition is imposed [23]:

$$\vec{\nabla}(\Phi) \cdot \hat{n} + \frac{\Phi}{d} = 0. \quad (2.16)$$

In this situations, usually, it is assumed that the flux will reach the zero value at a certain unknown distance far from the surface, represented in the equation by the term "d", which must be a positive function. When d is set equal to twice the diffusion coefficient, the Marshak boundary condition is retrieved, while, increasing the value of d, the reflector condition is approached (no outgoing current). The hard task is to estimate that distance, called "extrapolated length".

A different approach is given by the "albedo boundary condition". The albedo coefficient α is obtained as the ratio of neutron current entering the system and the leaving one at the boundary location (\vec{r}_B):

$$\alpha = \frac{J^{in}(\vec{r} = \vec{r}_B)}{J^{out}(\vec{r} = \vec{r}_B)}. \quad (2.17)$$

Therefore, when α is set equal to zero, no incoming current is expected from the outer medium (i.e. the surfaces where $\alpha = 0$ are free surfaces). Recalling the definition of neutron partial currents [24]:

$$\alpha = \frac{J^{in}(\vec{r} = r_B)}{J^{out}(\vec{r} = r_B)} = \frac{\frac{1}{4}\Phi + \frac{1}{2}D\vec{\nabla}(\Phi) \cdot \hat{n}}{\frac{1}{4}\Phi - \frac{1}{2}D\vec{\nabla}(\Phi) \cdot \hat{n}}. \quad (2.18)$$

Which, after some maths, turns to be an equation in the form of equation 2.16 where the extrapolated length depends on the albedo coefficient, in particular $d = 2D\frac{(1+\alpha)}{(1-\alpha)}$:

$$\vec{\nabla}(\Phi) \cdot \hat{n} + \frac{(1-\alpha)}{2D(1+\alpha)}\Phi = 0. \quad (2.19)$$

In the case in which the boundary surface is not a free surface, but a boundary which looks to the neutron source (for example the First Wall of ARC), it is possible to apply the definition of incoming partial current in order to impose a source term over the boundary, it can be done constructing a mixed boundary equation of the type:

$$\vec{\nabla}(\Phi) \cdot \hat{n} + \frac{1}{2D}\Phi = \frac{2}{D}J^{in}. \quad (2.20)$$

Some conclusive remarks regarding the assumptions required by Fick's law are mandatory. Since equation 2.12 is valid everywhere in the analyzed medium except within some mean free paths from the boundaries, the computed fluxes in those locations will be very sensitive of the extrapolation length value.

The uniform medium assumption can be relaxed, allowing the possibility of using diffusion theory to study multi-region problems, given that the absorption in the diffusive media is not prevalent with respect to the scattering phenomena, or at least, the variation in space of the ratio $\Sigma^{scat}/\Sigma^{abs}$ is constant [23].

Also the no source and the small variations of the flux with respect to the position assumptions can be relaxed in systems where absorption is negligible with respect of scattering.

The enable possibility of study multiregion problems gives rise to the need of a new kind of boundary condition: interface conditions. Interfaces are those surfaces where neutrons move from a medium to a different one, encountering different values of diffusion

coefficient and cross sections. In those locations, two are the conditions that must be satisfied:

- Continuity of the neutron flux

$$\Phi_{mediumA} = \Phi_{mediumB}. \quad (2.21)$$

- Continuity of normal component of the neutron current. Remembering that it is the current that gives informations on the number of neutrons that cross a surface in the unit of time, requiring that

$$\vec{J}_{mediumA} \cdot \hat{n} = \vec{J}_{mediumB} \cdot \hat{n}, \quad (2.22)$$

ensures that neutrons accumulation at the surface is not allowed. This condition, however, is not strictly connected with diffusion theory, but it is exact, in the sense that must be verified also in the transport theory

Up to this point a very small attention has been paid to the nuclear properties of the media. They describe the interaction of the neutrons with the media, depending not only on the composition of the material but also on temperature and other physical properties not relevant for this analysis (like porosity). With the aim of performing a multi-physics analysis, it is mandatory to allow not only the neutronics to have an impact on the thermal-hydraulic behaviour of the system (through the power deposition field), but also the reverse, i.e. to permit that the variation of the temperature field has effects on the distribution of the neutrons inside the system. This effect is made possible by the feedback of the temperature of the media on the nuclear properties, the so called thermal Doppler effect. It is connected to the dependency of the cross sections on the relative velocity between the neutrons and the nuclei, being the temperature of the media the macroscopical observable of the microscopic motion of the nuclei (thermal agitation), i.e. the higher the temperature the more rapid the vibrations of the nuclei that will produce the energy broadening of the cross sections.

Finally, defining the generic nuclear property Σ_x , the temperature dependence can be exploited as follows [30]:

$$\Sigma_x(T) = \Sigma_x(T_{ref}) + \alpha_{\Sigma_x} \log \left(\frac{T}{T_{ref}} \right). \quad (2.23)$$

Where α_{Σ_x} is the thermal Doppler coefficient of the nuclear property Σ_x and T_{ref} is the temperature at which the nuclear property has been computed.

2.3 Thermal-hydraulic modelling

The equations that govern the flow of fluids and their heat exchange processes are conservation equations. In particular:

1. The mass of the flowing fluid is conserved;

2. The momentum rate change is equal to the sum of all the forces acting on the fluid particles;
3. The energy rate change is equal to the sum of the contribution of additional rate of heat and the work rate done on the fluid particles.

While fluids are represented as continuum, to describe their behaviour, in terms of macroscopic measurable quantities, it is mandatory to solve the following conservation equation, computing the distribution of velocity, pressure and temperature.

The mass continuity equation states that the rate of increase of mass in a certain fluid system must be equal (i.e. be compensated) by the net rate flow of mass into it [25]:

$$\frac{\partial \rho}{\partial t} = -\vec{\nabla} \cdot (\rho \vec{v}). \quad (2.24)$$

The left side of the equation represents the time variation of the density, while the right side is called convective term and represent the net amount of mass that exits the fluid element.

The momentum equations [25] contain as additional unknowns the viscous stresses, that cannot be eliminated, appearing naturally in the mathematical derivation of the equations. Therefore, in order to solve the momentum equations, suitable models for stresses must be introduced. Each family of fluid requires a different shear model. Focusing on Newtonian fluids, it can be demonstrated that the viscous stresses are a linear combination of the deformation rates, which are related to the shearing linear deformation and the volumetric deformation, with the latter that is usually negligible with respect to the former. Defining μ as the dynamic viscosity and λ as the volume viscosity, the viscous stresses for Newtonian fluid become:

$$\tau_{ii} = 2\mu \frac{\partial v_i}{\partial x_i} + \lambda \vec{\nabla} \cdot (\vec{v}), \quad (2.25)$$

$$\tau_{ij} = \mu \left(\frac{\partial v_i}{\partial x_j} + \frac{\partial v_j}{\partial x_i} \right). \quad (2.26)$$

The introduction of the Newtonian fluid model into the momentum conservation equations, yields to the famous Navier-Stokes (N-S) equations:

$$\frac{\partial \rho \vec{v}}{\partial t} + \vec{v} \cdot \vec{\nabla} (\rho \vec{v}) = -\vec{\nabla} (p) + \rho \vec{g} + \vec{\nabla} \cdot (\mu \vec{\nabla} (\vec{v})) + \vec{S}_{mom}, \quad (2.27)$$

where it is clear that the total variation of momentum on fluid particles is produced by the summed effect of pressure, gravitational, viscous forces and the source term S_{mom} that collects external momentum source together with the shear depending term.

The following is the energy conservation equation, written in the form of the internal specific energy e [26]:

$$\frac{\partial \rho e}{\partial t} + \vec{v} \cdot \vec{\nabla} (\rho e) = -p \vec{\nabla} \cdot (\vec{v}) + \vec{\nabla} \cdot (k \vec{\nabla} (T)) + \hat{\pi} \cdot \vec{\nabla} (\vec{v}) + q_v'''. \quad (2.28)$$

Please, note that the term containing $\hat{\pi}$, which is the viscous stress tensor defined as $\hat{\pi} = \mu[\vec{\nabla}(\vec{v}) + (\vec{\nabla}(\vec{v}))^T] + \lambda(\vec{\nabla} \cdot \vec{v})\hat{I}$, when the Newtonian model is used, it turns out to be a dissipation function, usually denoted with the letter Φ . For completeness refer to [26] and [28].

Experimentally, it has been noted that above a certain value of Reynolds number (Re_{crit}) - an adimensional measure of the ratio between inertial and viscous forces - the flow patterns becomes chaotic [28]. Pressure and velocity change in an unpredictable way, showing a fully 3D fluctuations, even if the case in analysis presents symmetries. Usually this problem is addressed performing a decomposition of the variables:

$$\phi(t) = \langle \phi(t) \rangle + \phi^*(t) = \Phi + \phi^*(t), \quad (2.29)$$

where Φ is the constant, time averaged, value of the variable and $\phi^*(t)$ represents the time dependent fluctuations around Φ . This procedure is known as Reynolds decomposition.

In turbulent flows rotational structures develop, the so-called turbulent eddies. They are very heterogeneous, with very wide length and time scales. The characteristic of turbulence is an improved fluid mixing that produce effective mass, momentum and heat transfer throughout the flow. The eddies grow thanks to a mechanism of power extraction from the mean flow: the large eddies (inertia dominated) are the first formed, than they make smaller portion of fluid move, resulting in smaller eddies production, in a process known as energy cascade. From the Reynolds decomposition of the flow variables (\vec{v}, p), new "averaged" equations are derived, in which the most of the fluctuation terms disappear, since by definition, their time averaging is null:

$$\frac{\partial \tilde{\rho} \vec{V}}{\partial t} = -\vec{\nabla} \cdot (\tilde{\rho} \vec{V}), \quad (2.30)$$

$$\frac{\partial \tilde{\rho} \vec{V}}{\partial t} + \vec{V} \cdot \vec{\nabla}(\tilde{\rho} \vec{V}) = -\vec{\nabla}(P) + \tilde{\rho} \vec{g} + \vec{\nabla} \cdot (\tilde{\mu} \vec{\nabla}(\vec{V})) - \sigma_{app} + S_{mom}, \quad (2.31)$$

where σ_{app} represents the apparent stresses introduced naturally during the development of the equations. It represents the term of momentum that is convected in the flow by the fluctuating eddies:

$$\sigma_{app} = \sum_{i,j} \frac{\partial \langle v_i^* v_j^* \rangle}{\partial x_j}, \quad (2.32)$$

equations 2.30 and 2.31 represents the Reynolds Averaged Navier-Stokes equations (RANS), while the apparent stresses are the so called Reynolds stresses.

In a similar way to (N-S) equations, where it is mandatory to define a model for stresses, to resolve properly RANS equations it is mandatory to define a turbulence model for handling Reynolds stresses. Classically, turbulence models have been classified in base of the number of additional introduced equations to treat Reynolds stresses.

As one can be imagine, the more the additional equations, the more expensive will be the solution from a computational point of view.

Additional equations	Name of model
Zero	Mixing length model
One	Spalart-Allmaras model
Two	k- ε
	k- ω
Seven	Reynolds stress model

Table 2.2: RANS turbulence models.

A very intensively used model in the framework of nuclear reactors CFD analysis is the k-epsilon model, in its standard version or in some upgraded versions (such as the realizable k-epsilon) [30]. Its basic assumptions are that the effects of the viscous stresses on the core mean flow are connected to the ones of the Reynolds stresses, which increase with the increase of the mean rate of deformation. The main advantage of this turbulence model is that has the capabilities to take into account the production and destruction of turbulence as well as its transport, both due to convection and diffusion, with a relatively low computational resource request. More than a century ago, Joseph Valentin Boussinesq introduced the idea that the Reynolds stresses could be proportional to the deformation rates. He proposed a definition similar to 2.26, which is characterized by the assumption that the deformation rate is uniform in all the directions:

$$\tau_{ij} = \mu_t \left(\frac{\partial V_i}{\partial x_j} + \frac{\partial V_j}{\partial x_i} \right) - \frac{2}{3} \rho k \delta_{ij}. \quad (2.33)$$

The new introduced turbulent variables are the kinetic specific turbulent energy $k = 0.5(\langle v_x^{*2} \rangle + \langle v_y^{*2} \rangle + \langle v_z^{*2} \rangle)$ and the turbulence viscosity μ_t , which is considered isotropic and for which a formulation based on dimensional analysis can be obtained:

$$\mu_t = \rho C_\mu \frac{k^2}{\varepsilon}. \quad (2.34)$$

With these concepts kept in mind, it is possible to derive [Malakkakasera] the transport equations for the characterizing variables of the model: kinetic energy (k) and its dissipation rate (ε) :

$$\frac{\partial \rho k}{\partial t} + \vec{\nabla} \cdot (\rho k \vec{V}) = \vec{\nabla} \cdot \left(\frac{\mu_t}{\sigma_k} \vec{\nabla}(k) \right) + 2\mu_t S_{ij} \cdot S_{ij} - \rho \varepsilon, \quad (2.35)$$

$$\frac{\partial \rho \varepsilon}{\partial t} + \vec{\nabla} \cdot (\rho \varepsilon \vec{V}) = \vec{\nabla} \cdot \left(\frac{\mu_t}{\sigma_\varepsilon} \vec{\nabla}(\varepsilon) \right) + C_{1\varepsilon} 2\mu_t S_{ij} \cdot S_{ij} \frac{\varepsilon}{k} - C_{2\varepsilon} \rho \frac{\varepsilon^2}{k}. \quad (2.36)$$

In the last two equations, the terms appearing represent what has been previously stated. The first term corresponds to the time rate of change of the turbulent properties; the second one is the convection contribution; the third the diffusion one; the fourth is the production rate of k or ε and finally, the last term (it has a negative sign in front of) is the destruction rate. Please note how the destruction of the kinetic energy depends on ε . The two last phenomena (production and destruction) are intimately linked, in fact

in ε equation they are the same of the k equation, just scaled of some factors. In the following table the adjustable constants appearing in eqns. 2.34, 2.35, 2.36 are reported:

C_μ	σ_k	σ_ε	$C_{1\varepsilon}$	$C_{2\varepsilon}$	κ	E
0.009	1.00	1.30	1.4	1.92	0.41	9.80

Table 2.3: $k - \varepsilon$ adjustable parameters.

Some particular attention must be reserved to the flow next to the walls. Defining a particular Reynolds number - with the usual aim (represents the ratio between inertia and viscous forces) - which varies with the distance from the wall (y), at some point Re_y must be equal to unity. This means that the viscous phenomena become comparable to the inertia ones, and even more important approaching further the solid surface: near wall flow is characterised by viscous forces, independently by mean core flow properties. In fact, from dimensional analysis, it can be shown that:

$$u^+ = \frac{V}{u_\tau} = f\left(\frac{u_\tau y}{\nu}\right) = f(y^+), \quad (2.37)$$

where u_τ is the friction velocity obtained by $u_\tau = (\tau_{wall}/\rho)^{0.5}$.

The $k-\varepsilon$ model, at high value of standard Reynolds number, does not require to solve directly the equations 2.35 and 2.36, in fact when $y^+ \in [30,500]$ and the dissipation rate of the turbulence variables compensate their production, some wall functions can be used:

$$u_\tau = \frac{V}{u^+} = \frac{V}{\frac{1}{\kappa} \ln Ey^+}, \quad (2.38)$$

$$k = \frac{u_\tau^2}{C_\mu^{0.5}}, \quad (2.39)$$

$$\varepsilon = \frac{u_\tau^3}{\kappa y}. \quad (2.40)$$

For low values of Re , instead, are the main $k-\varepsilon$ that are directly modified, they can be seen in [28].

2.4 Finite volume modelling

The Finite Volume Method (FVM) is a computational method which converts partial differential equations (PDEs) representing conservation phenomena, into discrete algebraic equations. The discretization process acts also on the domain: if the PDEs operate over differential volumes, the algebraic equations operate over finite volumes (in this work sometimes referred as cells, FV, discrete domains, with no actual distinction). The ensemble of discrete finite volumes takes the name of mesh (FVM allows the use of unstructured meshes), over which the equations are solved.

The founding idea of FVM is that the entering fluxes in a FV, must be equal to the sum of the fluxes that leave that FV towards adjacent cells. Here, the need of limit the range on conservation equations.

FVM consists on two steps: in the first, the real physical domain is discretized in meshes, whose cells must not overlap each other, then the conversion of PDEs into sets of algebraic balance equations is performed through the conversion of the real physical terms into fluxes.

The solution of the problem consist in the computation of the variables of interest (let's indicate with ϕ the generic continuous physical variable and with $\tilde{\phi}$ the discretized one) in predefined points of the meshes (grid nodes). For example, taking as reference the generic steady state conservation equation of the type [27]:

$$\vec{\nabla} \cdot (\rho \vec{v} \phi) = \vec{\nabla} \cdot (D \vec{\nabla}(\phi)) + S, \quad (2.41)$$

where, in order, are represented convection, diffusion and source term. Integrating over the volume domain and applying the Gauss theorem to the first two terms:

$$\oint (\rho \vec{v} \phi) \cdot d\vec{\Sigma} = \oint (D \vec{\nabla}(\phi)) \cdot d\vec{\Sigma} + \int S d\vec{r}. \quad (2.42)$$

It is possible to define a convection and a diffusion fluxes, such that:

$$\oint \vec{J}^{conv} \cdot d\vec{\Sigma} + \oint \vec{J}^{diff} \cdot d\vec{\Sigma} = \int S d\vec{r}. \quad (2.43)$$

Moving, at this point, from the comprehensive to the cell-localised point of view, each integral can be seen as the sum of a set of integrals on the surfaces of the discrete volumes. With the aim of proceeding with the discretization process, Gauss quadrature formula can be used to evaluate the integrals, reaching the final stage of the integral manipulation:

$$\sum_{faces} \sum_{i=1}^{N_{points}} \left(w_i (\vec{J}^{conv,i} + \vec{J}^{diff,i}) \cdot d\vec{\Sigma} \right) = \sum_{i=1}^{N_{points}} \left(w_i \tilde{S}^i d\vec{r} \right), \quad (2.44)$$

where i is the index of the integration points and w_i the Gauss weights.

At this point, the missing part is the explicit discrete form of the fluxes written in terms of neighbour cells. A linearization process is performed, so that:

$$\vec{J} \cdot d\vec{\Sigma} = \alpha_{center} \phi_{center} + \alpha_{face} \phi_{face} + \phi_{non,linear}, \quad (2.45)$$

where the α coefficients depend on the discretization schemes, while $\phi_{non\ linear}$ is the term that cannot be expressed by means of ϕ_{face} or ϕ_{center} .

2.4.1 Finite Volumes and OpenFOAM

OpenFOAM (OF) stands for Open-source Field Operation And Manipulation. It is a C++ object-oriented framework that can be used to develop the so called "applications". An application is an executable which relies on a set of libraries (more than one hundred) contained in the source code of OF, usually used to develop computational tool to solve continuum mechanics problem through the use of finite volume approach.

The history [15] of OpenFOAM is, therefore, characterized by an extensive use in the Computational Fluid Dynamics field. The first appearance of a similar tool was in 1989, thanks to Henry Weller, who created the FOAM code during his years at the Imperial College of London. In 2004, finally, the same Weller, together with Chris Greenshields and Mattijs Janssens, decided to release an open-source version of the code [14], with the current name OpenFOAM. Today, OF is distributed with a General Public Licence (GPL) allowing anybody to use it and modify the source code, contributing to its development and ensuring a continued updated use.

I would like to focus on the key aspect that characterize OpenFOAM and differentiates it from the other FV codes: the fact that it is a free, open-accessible code permits a widespread of applications, exploiting its flexibility and allowing users from all over the world to develop their own projects while sharing their experience and their know-how. Beyond OpenFOAM exists a community made of people who are simultaneously users and developers. This is what research should be based on: a free, genuine sharing of skills and expertise.

Mainly, two different kind of applications exist: solvers and utilities. The former are the executables that actually solve the problems (each solver addresses a specific problem), while the latter perform useful tasks on field data.

One of the most powerful features of OpenFOAM is the possibility of express operators in a almost human spoken language. For example, if one would implement a solver which discretizes equation 2.41, the corresponding code would be:

Listing 2.1: Implementation of equation 2.41 in OpenFOAM.

```
(
  fvm::div(rho*v, phi)
  - fvm::laplacian(D, phi)
  ==
  fvc::(S)
)
```

In this simple example it is shown how the two types of operators `fvm` and `fvc` are called. They are containers for the static functions `finiteVolumeMethod` and `finiteVolumeCalculus` representing respectively, implicit and explicit operators. In the following figure (fig. 2.4), extracted from OpenFOAM guide [29], are reported all the operators present inside the reference libraries.

Many tools are available for the process of mesh generation. Some of them are present in all the different packages of OpenFOAM (`snappyhexmesh` and `blockmesh`), others are available only in the `.com` distributions or can be added manually after the installation of the basic package of OF.

The visualization and the manipulation of the data is usually performed with an external open-source application, named `Paraview`, that is usually contained in the basic OpenFOAM package. The three different steps in the OF workflow are represented in fig. 2.5.

Everybody can develop its own solver, compile it and use it, also without a C++ coding background. In this thesis the `nemoFoam` was developed starting from a simplified version of the `msfrFoam` code [30] (namely `msfrDemoSimpleFoam`) while the

Term description	Implicit / Explicit	Text expression	fvm::/fvc:: functions
Laplacian	Imp/Exp	$\nabla^2 \phi$ $\nabla \cdot \Gamma \nabla \phi$	laplacian(phi) laplacian(Gamma, phi)
Time derivative	Imp/Exp	$\frac{\partial \phi}{\partial t}$ $\frac{\partial \rho \phi}{\partial t}$	ddt(phi) ddt(rho, phi)
Second time derivative	Imp/Exp	$\frac{\partial}{\partial t} \left(\rho \frac{\partial \phi}{\partial t} \right)$	d2dt2(rho, phi)
Convection	Imp/Exp	$\nabla \cdot (\psi)$ $\nabla \cdot (\psi \phi)$	div(psi, scheme)* div(psi, phi, word)* div(psi, phi)
Divergence	Exp	$\nabla \cdot \chi$	div(chi)
Gradient	Exp	$\nabla \chi$ $\nabla \phi$	grad(chi) gGrad(phi) lsGrad(phi) snGrad(phi) snGradCorrection(phi)
Grad-grad squared	Exp	$ \nabla \nabla \phi ^2$	sqrGradGrad(phi)
Curl	Exp	$\nabla \times \phi$	curl(phi)
Source	Imp Imp/Exp†	$\rho \phi$	Sp(rho, phi) SuSp(rho, phi)

Figure 2.4: Operators available in OpenFOAM [29].

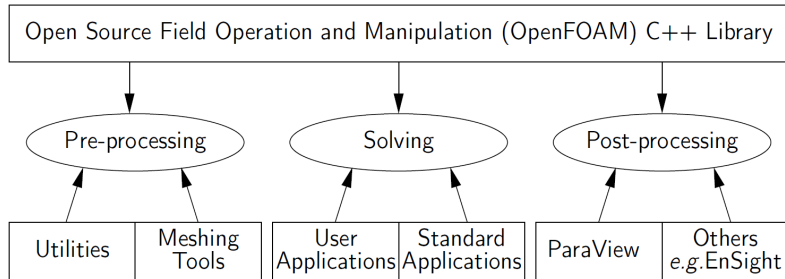


Figure 2.5: Workflow steps of an OpenFOAM simulation [29].

thermal-hydraulic code *my_chtMultiRegionFoam* is a slightly modified version of the well established *chtMultiRegionFoam*, one of the official solver of OF.

Chapter 3

nemoFoam benchmark

The nemoFoam code represents the main contribution produced in the development of this work. It is a Finite Volume tool which solves the multi-group diffusion equations in multiple regions. The number of energy groups is not predefined and it is selected by the user with a parameter. It has been developed with the aim of being suitable for fusion and for fission applications. For this reason in the neutron fluxes computation module it takes into account of possible fission terms, neutron precursors and decay heat precursor. Since the main objective of thesis is the multi-physics analysis of the blanket of a fusion reactor, nemoFoam code computes the power deposited by neutrons in the media due to three different phenomena: fission power source, decay heat and kerma. The code is implemented as a transient code, but can switch to steady state problems by selecting the appropriate time scheme (steady state). nemoFoam has been developed based on the msfrDemoSimpleFoam, a simple variant of the msfrFoam, a multiphysics tool for molten salt reactors developed at the Politecnico di Milano [30]. The main differences with respect to msfrDemoSimpleFoam are the possibilities of treating a multiregion problem and the introduction of the kerma power deposition. New boundary conditions (BC) were implemented such as the albedo BC and the imposed incoming neutron current BC, both inside the boundary condition called PhiBC. Being a multiregion solver, also the interface condition was implemented, to guarantee, as stated in chapter 2, the continuity of flux and of the normal current. nemoFoam has been uploaded on github and can be consulted at [31].

In its core structure, nemoFoam is not a particularly complex solver, it is otherwise quite linear and schematic. What is much less user-friendly is the structure of the case folders and of the input files that must be fed to the solver, to implement neutronic properties, initial and boundary conditions.

Before applying the neutronic tool to the thesis case study, it has been studied a benchmarking problem, in order to compare the computed solution with the one produced by the Serpent [32] Monte Carlo particle transport code.

3.1 Benchmark setup

In analogy with the shape of the plasma in a tokamak, the analysed case consists in two hollow tori (fig. 3.1) of different materials, i.e. the inner one is made of Inconel718 (red one), the outer one of FLiBe (blue one in transparency).

The CAD model has been produced by means of FreeCAD, an "open-source parametric 3D modeler" [33], and exported in STEP format, then it has been loaded into Salome, an "open-source pre-processing software" [34], to define the patches and produce the FMS file required by cfMesh [35], the selected meshing tool.

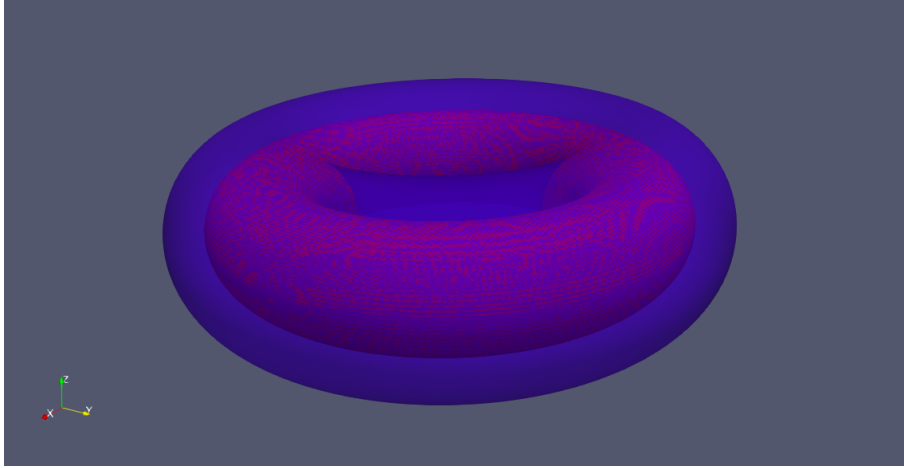


Figure 3.1: CAD model of the benchmark case study.

The relevant dimensions of the bodies are represented in figure 3.2 which shows a section of the torus on a (r,z) plane, in particular R_0 is set to be 5 m, r_1 is 0.5 m, r_2 is 1.5 m and r_3 is 2.5 m.

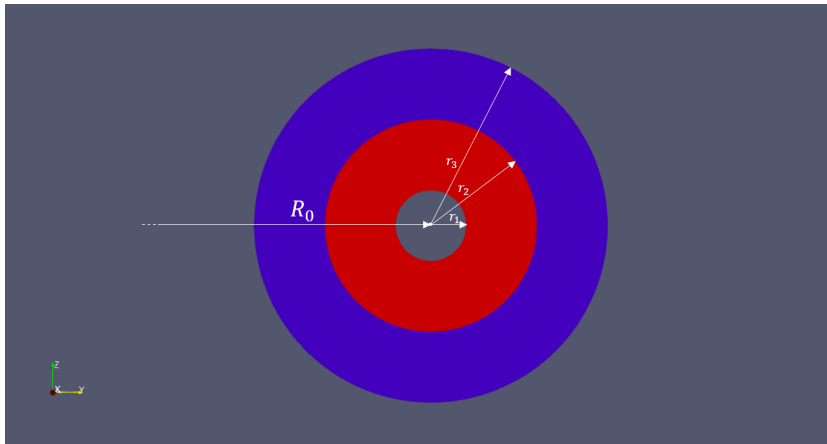


Figure 3.2: Poloidal section of the case study CAD model and reference measures.

Regarding the choice of the number of the energy groups taken into account in the

analysis, in order to balance accuracy of the solution and computational power required, six groups are considered, with the subdivision showed in the table 3.1.

Energy groups	1	2	3	4	5	6
Upper threshold [MeV]	2.0E+01	1.0E+01	1.0E+00	1.0E-01	1.0E-02	1.0E-04
Lower threshold [MeV]	1.0E+01	1.0E+00	1.0E-01	1.0E-02	1.0E-04	0.0E+00

Table 3.1: Energy groups subdivision.

The nuclear properties (i.e. diffusion coefficients, cross sections and kermas) for each group are computed by means of the Serpent code.

In the probabilistic simulation, the source of neutrons is uniformly distributed in the inner empty volume (representing the plasma volume) and its rate is set to be equal to $1.86\text{E}+20$ neutrons/s, all the neutrons are isotropically generated with an energy of 14.1 MeV, so, given the group subdivision in the deterministic analysis, they will belong to the first one. Since nemoFoam is a diffusion solver, it cannot resolve the propagation of neutrons in a very rarefied medium (as plasma is); instead of defining a plasma volume where neutrons are generated, the resulting incoming neutron currents have been computed by means of Serpent and have been used as boundary condition at the Inconel torus inner surface (at $r = r_1$). It is important to note that currents for all the groups are imposed, not only for the first one (the neutrons coming from the source belong to this group), in order to take into account the fact that the surface under consideration is a reentrant type surface, i.e. a surface of a medium in contact with the vacuum such that exiting neutrons can enter again in the medium [23]. At internal boundaries, i.e. the interface between Inconel and FLiBe ($r = r_2$), interface boundary condition are imposed, while at external boundaries, i.e. at $r = r_3$, the free surface boundary condition has been imposed.

The meshes of the two different torus have been produced individually by means of cfMesh, through *cartesianMesh*, the selected meshing workflow, which produces mainly hexahedral cells and polyhedral ones only in regions between zones of different cell sizes, i.e. in the transition regions [35]. For both torus a common maximum cell size of 0.1 [m] has been imposed, then, for the Inconel domain an additional progressive relative refinement has been performed locally from the plasma facing surface (the one at $r = r_1$) in out-coming radial direction. In particular, four levels of refinements have been studied, each of them consisting in halving the maximum cell size of the refined region with respect to the value corresponding to the previous refinement. The rationale behind this type of the mesh refinement analysis is that being the problem purely diffusive, with no neutron multiplication inside the media, the steeper gradients of the neutron fluxes are expected to be near the surface in contact with the source, so that zone is the area to pay more attention to.

The grid independence analysis has been carried out looking at the value of the power deposited in the two torus individually, called respectively $P_{Inconel}$ and P_{FLiBe} .

In the table 3.2 it is shown a summary of the different characteristics of the mesh refinements and the results obtained in the analysis, while in the fig. 3.3 the trend of the

computed values of power are plotted with respect to the level of refinement of the mesh.

Refinement level	Max cell size [cm]	$P_{Inconel}$ [W]	P_{FLiBe} [W]
0	10	1.0068E+08	4.2010E+05
1	5	1.0687E+08	4.1734E+05
2	2.5	1.0878E+08	4.1595E+05
3	1.25	1.0929E+08	4.1517E+05
4	0.625	1.0943E+08	4.1475E+05

Table 3.2: Refinement characteristics of the Grid Independence Analysis.

As the figure 3.3 shows, the deposited powers are converging, in particular, the relative error in the computed power between 3 and 4 levels of refinement is respectively 0.2% for the Inconel torus and 0.1% for the FLiBe one, therefore, for the purpose of the benchmark, convergence can be considered reached. Given this, in order to reduce the computational cost, the mesh obtained with 3 levels of refinement is chosen as reference.

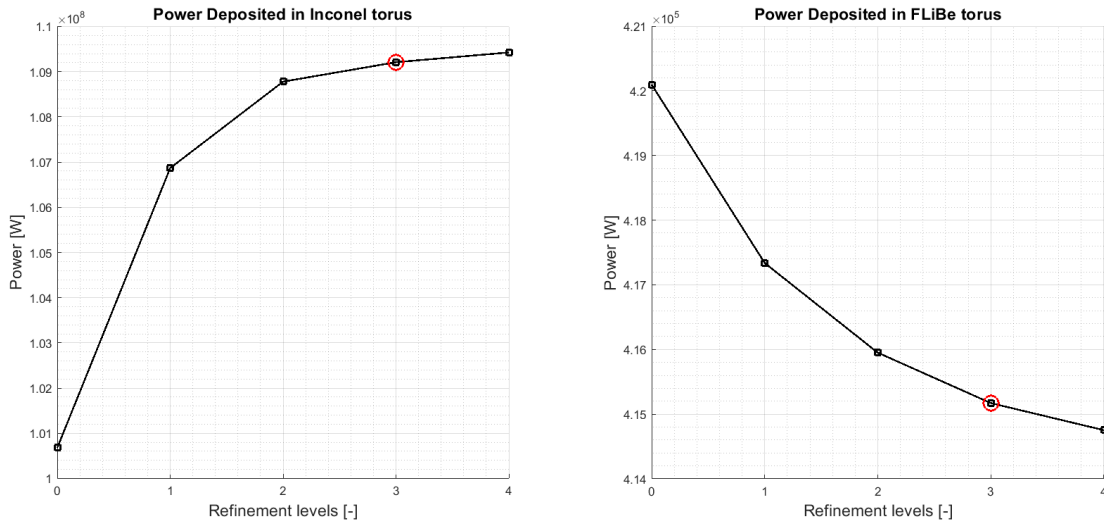


Figure 3.3: Convergence of power in the Grid Independence Analysis.

Fig. 3.4 reports the selected complete mesh, a planar poloidal section of it and a focus on the refined zone, where it is possible to appreciate the progressive refinement of the base size of the cells.

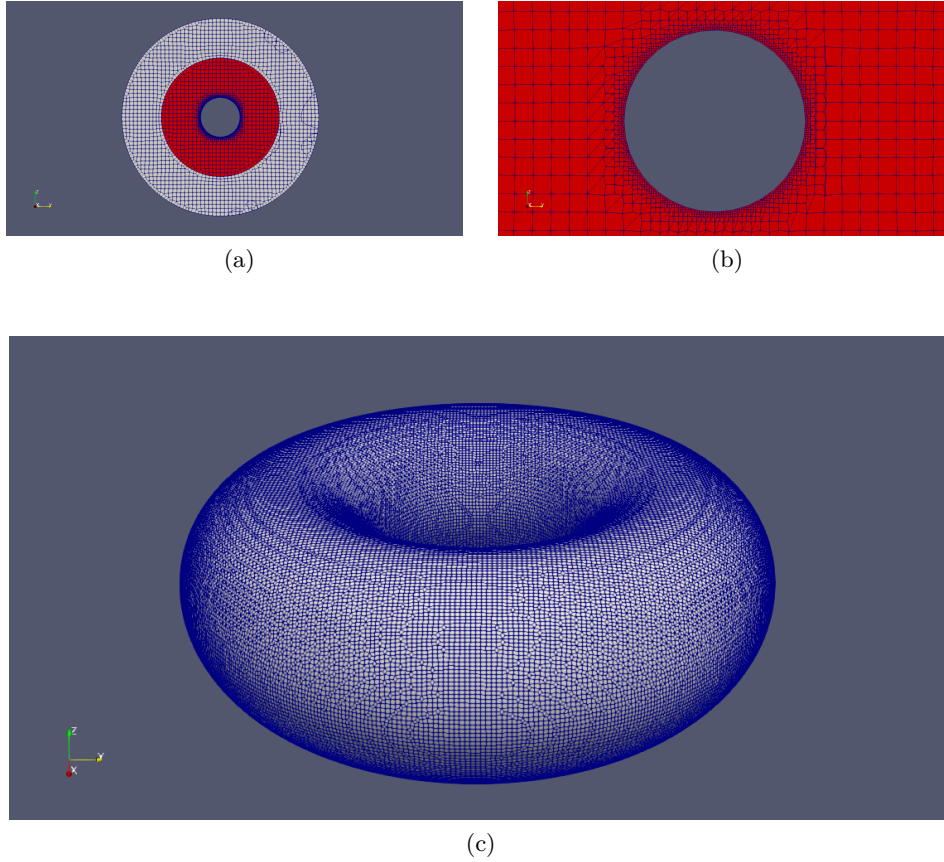


Figure 3.4: Mesh of the benchmark case corresponding to the refinement level 3.

3.2 Benchmark results

In this section the results of the analysis are shown in three different steps: the first focuses on the qualitative general behaviour of the solution by reporting the flux map fields for each energy group on the poloidal section of figure 3.4; then a quantitative analysis is conducted, still from a general point of view, presenting a comparison of the spectrum predicted by nemoFoam and by the Monte Carlo code Serpent; finally, a local quantitative comparison is presented with the comparison between the fluxes computed by the two codes as function of the radial coordinate on the very same poloidal section.

An additional note must be added on the Monte Carlo simulations: the procedure requires, as input from the user, the number of generated particles N_0 that the software will use to compute the solution, which will be very sensitive on this parameter. For the case in analysis, the total number of generated particles in the Monte Carlo simulation is set to $1\text{E}+8$ [neutrons].

Figure 3.5 shows the six neutron flux maps on a poloidal section of the torus. The spatial behaviour fits the expected exponential decay that can be observed in the case of any purely diffusive problem, with no internal source but an imposed neutron current

at the inner surface. The incoming neutrons (at $r = r_1$) while interacting with the medium can only be absorbed or scattered. In the former case they are "lost" and do not contribute anymore to any flux, in the latter case they release energy to the media and slow down, if their energy decreases below the lower threshold of the belonging group before the collision with the nucleus, they change energy group and contribute to lower velocity fluxes.

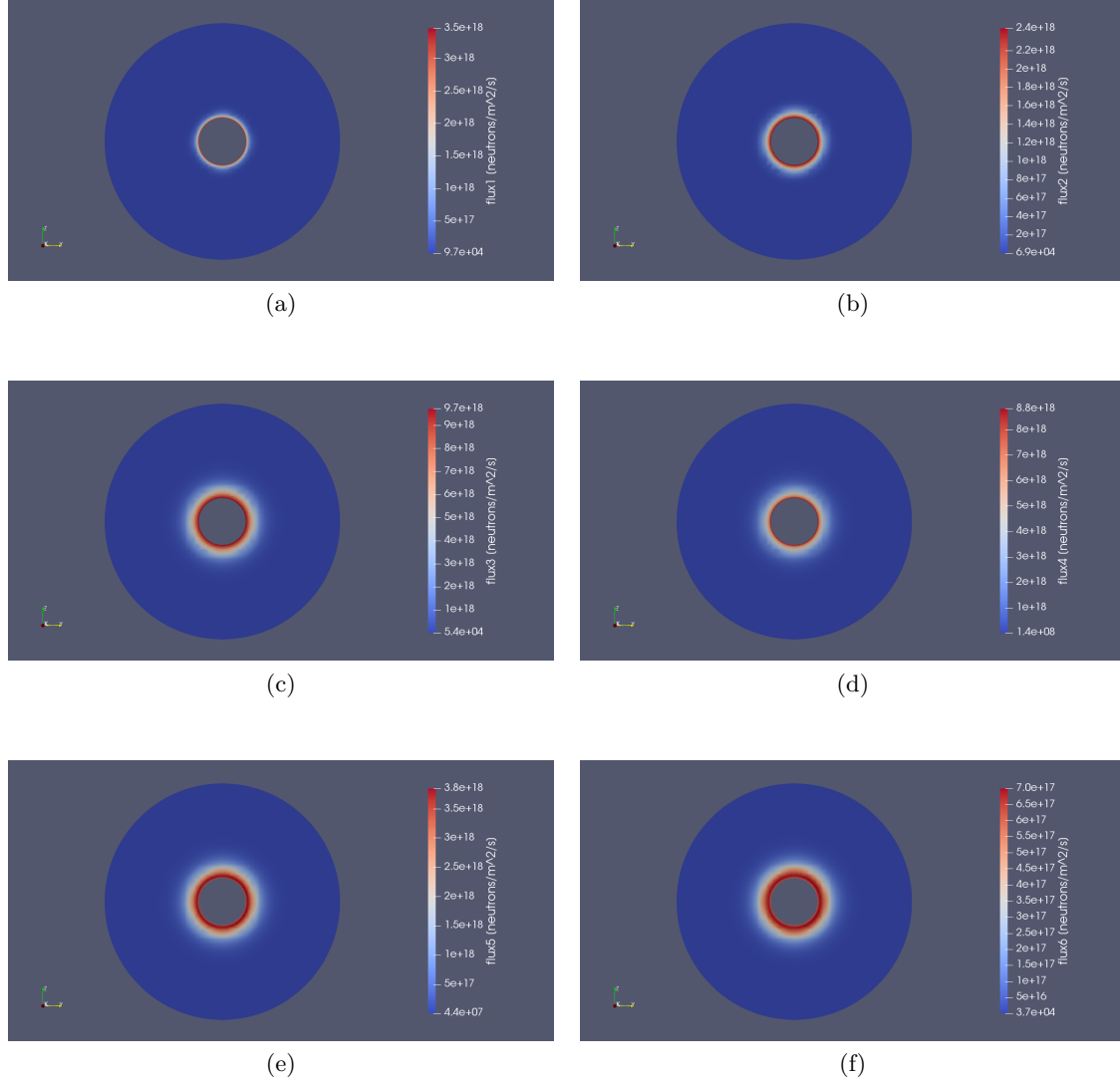


Figure 3.5: Neutron flux map on a 2D poloidal section (flux of energy group 1 is the first in the top left sector, flux of energy group 6 is last in the bottom right sector).

Figure 3.6 shows the spectrum of the fluxes in the two different media. The neutron flux spectrum describes the distribution of the neutrons over the discretized energies [?]: since neutrons are generated with very high energies (14.1 MeV), as said previously,

they slow down interacting with the nuclei of the medium in which they propagate. The characteristics of the process depend on the properties of the medium, on the arrangement and the geometry of the system and from the source of the neutrons. Any information related to this process cannot be obtained directly from the flux spatial map itself, but from the spectrum.

The largest differences between nemoFoam and Serpent appear to be in the more energetic groups in the FLiBe torus, instead of the Inconel torus where the spectrum trends are very similar. The reason for this fact can be understood easier if the radial flux distribution is considered.

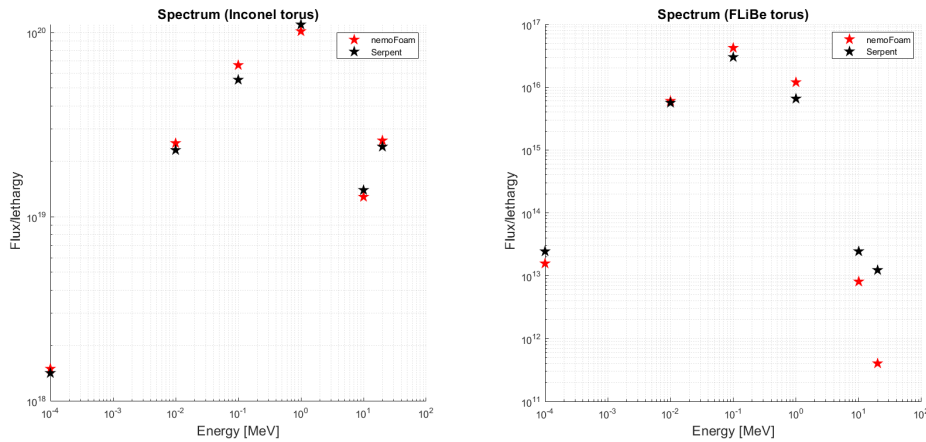


Figure 3.6: Neutron spectrum in the Inconel718 region and in the FLiBe region. The error bars are not visible because the relative error is too low.

The trend of the neutron fluxes computed by nemoFoam are overall in good agreement with the Serpent ones as the figures 3.7 and 3.8 show.

It is significant to highlight the fact that the Serpent simulation obtained few statically meaningful results in the FLiBe torus, i.e. far from the source where the few survived neutrons (to the interactions with Inconel nuclei) arrive. Please, remember the setup of this analysis: the Inconel torus has a minor radius of 1 meter, therefore its shielding is extremely effective and, given the chosen value of N_0 , the fast neutrons that arrive in those zones are not enough to produce a result. This is the reason for which, according to Serpent, there are no neutrons (or a few) of the most energetic groups in the FliBe torus, as shown effectively in the logarithmic scale plot (fig. 3.8). Increasing the value of the total number of the generated neutrons would produce better results, but for the objective of this benchmark it would have required a too high computational cost. In figure 3.8 is also easy to note that every trend changes across the interface (at $r = r_2$) very abruptly and with some jumps. It seems that the flux is not continuous in those locations, even if the boundary conditions implement the continuity of the flux and of the net number of neutrons that crosses the surface, as required by the theory in the section 2.2. The

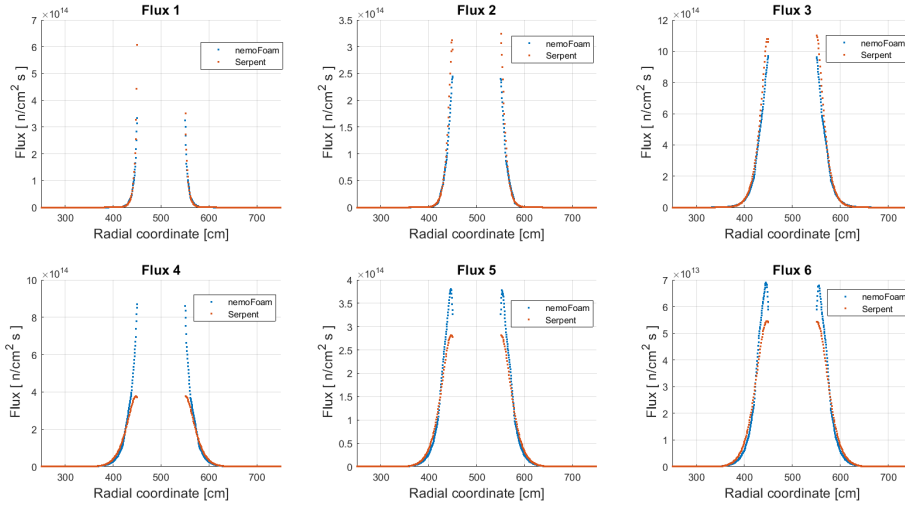


Figure 3.7: Neutron fluxes in linear scale for the six energy groups. The error bars are not visible since the absolute error is too small, because where the flux is small the statistical error is large and vice versa. Therefore overall the error bar is too small to display.

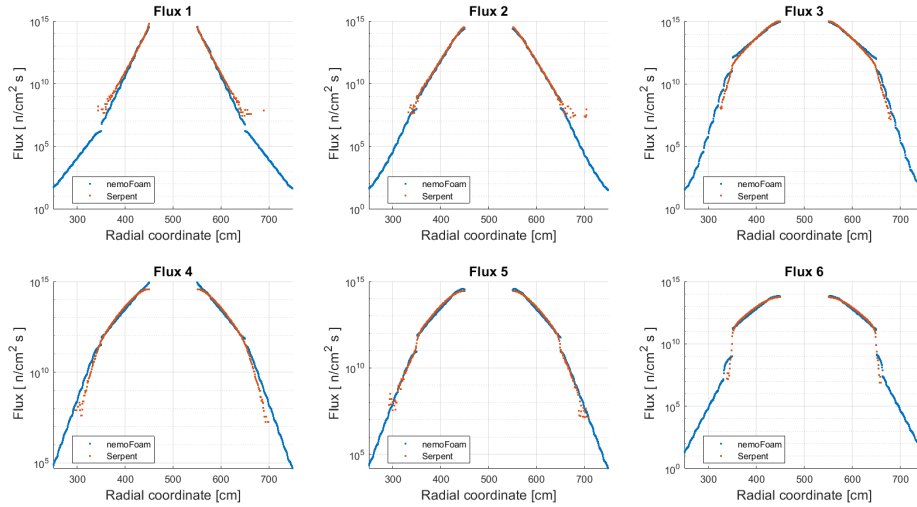


Figure 3.8: Neutron fluxes in logarithmic scale for the six energy groups. The error bars of the Serpent simulations are not shown to privilege the good visibility of the profiles.

cause of the shown behaviour is addressable to the bad treatment of the interface from the meshing point of view. In fact, with the addition of few boundary layers, on each side of the interface, the unexpected jump disappears and the fluxes become continuous, as shown in figure 3.9.

However, the not properly resolved mesh at the interface affects only the amount of

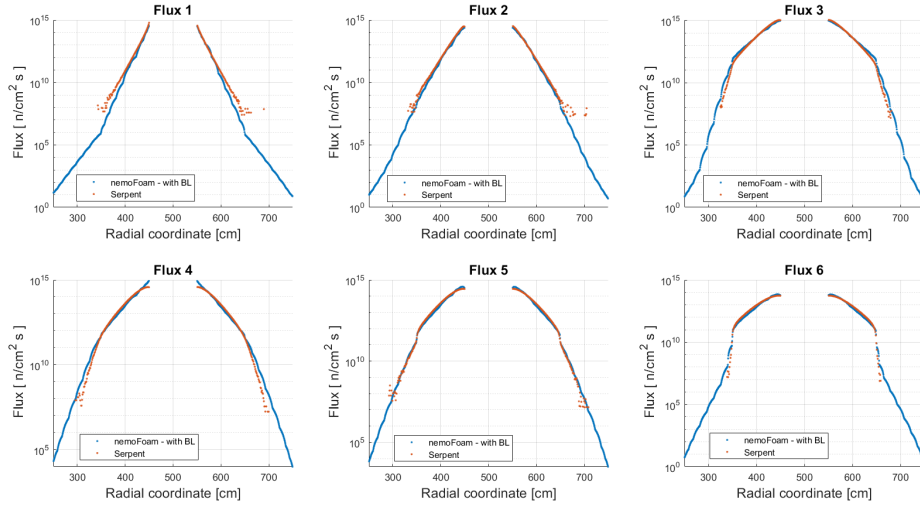


Figure 3.9: Neutron fluxes in logarithmic scale for the six groups after the addition of the boundary layers. The error bars of the Serpent simulations are not shown to privilege the good visibility of the profiles.

power deposited in the second medium, as expected. In particular, from the comparison presented in table 3.3 where are reported the power deposited in the two torus computed by the Monte Carlo and by the nemoFoam simulations (one with boundary layers and one without) it is possible to find a good agreement in the Inconel torus, but not in the FLiBe one. This difference can be addressed to the fact that since the Monte Carlo simulation does not produce statistically meaningful results for the more energetic groups in the FLiBe torus, i.e. according to the probabilistic code no power is there deposited, the total amount of it is lowered, as if the overall deposition of power was "incomplete".

	Region	Serpent	nemoFoam - no BL	nemoFoam - with BL
Power [W]	Inconel718	1.05E+08	1.09E+08	1.09E+08
	FLiBe	3.32E+05	4.15E+05	4.29E+05

Table 3.3: Comparison of the power deposition in the benchmark case.

The nemoFoam code demonstrates the capability of computing the fluxes through the whole domain, also in the regions where the fluxes are low, i.e. few survived neutrons reached that location. This aspect is of relevant importance, especially, if the computational times needed by the two procedures (with the same computational power) are taken into account: Serpent produced the shown results in 18 hours, nemoFoam in less than one hour.

Chapter 4

Simulation workflow

4.1 CAD production

The geometry of the blanket of the ARC reactor, as seen in the section 2.1, is very complex, involving multiple layers of different materials and many inlets and outlets. Since no CAD model is currently available in the accessible material for ARC, a basic geometry has been built from scratch by means of FreeCAD. The starting point of the 2D sketch has been the few information available, such as the major radius of the torus of 3.3 [m] [7] and then integrated with the measures extracted by [21]. The resulting sketch is reported in the figure 4.1, where the multi layers are already present with the thickness defined by the figure 2.1. Being the structure axial-symmetric, it was sufficient to generate a 10° rotation solid.

In the table 4.1 are reported the volumes of each region for the full 360° rotation solid, to be compared with the reference values reported in [7]. As it is possible to see, there are some differences, mainly for the blanket region. Since the design of ARC is currently under development and improvement, this fact has been considered not of relevant importance. An increase in the total power deposition is however expected, leading to a conservative analysis.

	Volumes [m^3]	
	FreeCAD	Reference [7]
First Wall	0.324	0.35
Inner VV	3.26	3.50
Cooling Channel	6.55	7.04
Neutron Multiplier	3.30	3.55
Outer VV	9.98	10.7
Blanket	341	241

Table 4.1: Comparison of the volumes of the components of the ARC blanket obtained in this work with the reference.

Later on, additional channels were added to the CAD to take into account inlet, outlet

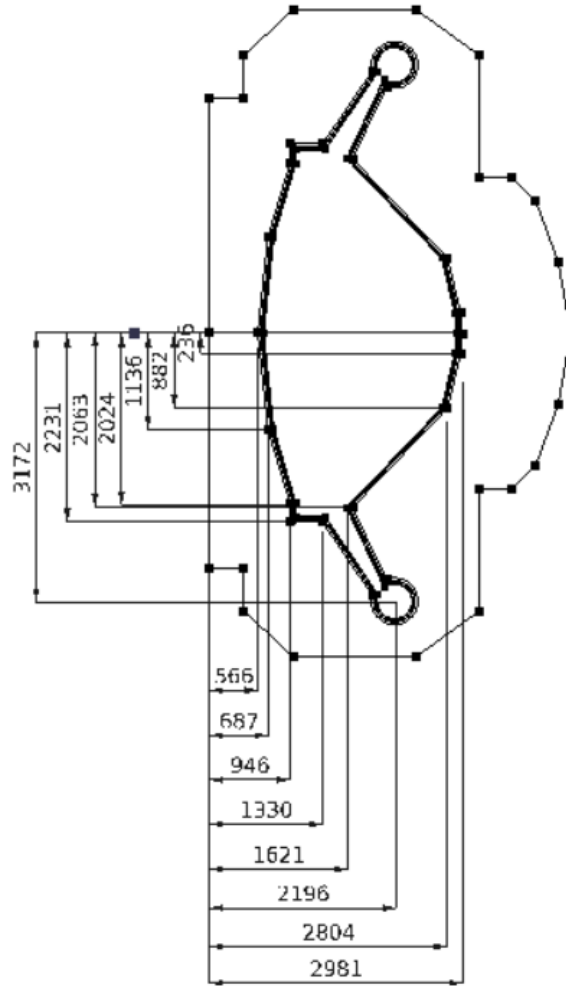


Figure 4.1: 2D sketch of the blanket tank and of the layers produced in FreeCAD for this work. Measures are expressed in millimeters [mm].

and the port of communication between the cooling channel and the blanket tank. In particular it has been taken as reference the geometry reported in [21]. The connection between the channel and the blanket tank has been simplified with respect to the real layout (refer to fig. 2.2), consisting in just one port in the inferior portion of the geometry. Under this hypothesis, the flow is expected to split in two, one stream going to the upper divertor and then going down through the "outer side" of the channel (named "outboard"), while the other stream going directly to the port through the inner side of the channel (named "inboard"). An additional simplification has been performed, joining the solid layers in two distinct regions, following the rationale of homogenization. This choice has been carried out to reduce the computational cost of the meshing process and of the calculations, mainly because of the tungsten layer, which being 1 mm thick with a volume

of 0.009 m^3 would have required a huge amount of cells ($1.31\text{E}+08$ cells) for a region of negligible impact for the thermal-hydraulic analysis. At the end of the homogenization process three regions were produced: one composed by the tungsten layer and the inner vacuum vessel, one obtained by the union of the outer vacuum vessel and the beryllium layer and one relative to the fluid domain (cooling channel and blanket tank). These modifications result in a slightly different CAD, which characteristics are highlighted in the following figure 4.2 reporting (please note that, for clarity, only the fluid domain is shown), a focus of the inlet patch and of the connection port with the blanket.

Finally the geometry files have been exported singularly in STEP format and uploaded in Salome. Salome allows the users to manipulate the geometry files (in principle it also consents to produce the geometry directly in a built in CAD module) and export them in a format readable by the meshers, namely a .fms or .stl files. In particular the former one is the preferred format of the input file of cfMesh [35] since in this format, all the information related to the geometry are saved in the file itself (such as the feature edges) while in the .stl file they are not. The most common activity usually performed in Salome is the naming of the patches of the geometry, for example defining a patch corresponding to an inlet as "inlet", very useful for the definition of the boundary conditions and of the type of the patch in OpenFOAM. An interesting feature of Salome is that, since is written in python, it allows to use external scripts for processing the geometry files. In particular, using a combination of two scripts of the cfMesh package (*extractFeatureEdges.py* and *salomeTriSurf.py*) it is possible to extract the information relative to the feature edges of the geometry, then to the triangularization file and export it. This step is very useful for the meshing step, ensuring a good resolution of the edges of the mesh. Therefore, the final files produced by Salome are .fmd that contain 2D triangularizations of the geometries with the naming of the patches and the information on the feature edges.

4.2 Meshing

cfMesh is a tool able to mesh in a single domain only, for this reason each region has been meshed by itself. This aspect, if on one side provided a great flexibility on the choice of the parameters for each mesh, on the other, required a careful re-definition of the topology of the communicating patches, right before the beginning of the simulations.

In particular, each contiguous patch has been redefined as type *mappedWall*, choosing as sample mode *nearestPatchFaceAMI*, by means of the command *createPatch* which uses the information contained in the file *createPatchDict* located in each directory of the single regions in the *system* directory of the simulation case. The rationale behind the choice of the sample mode is motivated by the characteristics of the sampling: with the defined workflow OpenFOAM samples the value on the face of the nearest cell of the communicating patch defined in the dictionary, allowing to use not conformal patches (i.e. the grid on the patch can be different) and using the Arbitrary Mesh Interface (AMI) interpolation, which allows sampling on disconnected but contiguous mesh regions [29].

The decisions made during the meshing workflow privileged a good compromise between accuracy and computational time. Thanks to the structure of the developed multi-physics tool it has been possible to solve the neutronic (NE) and the thermal-hydraulics

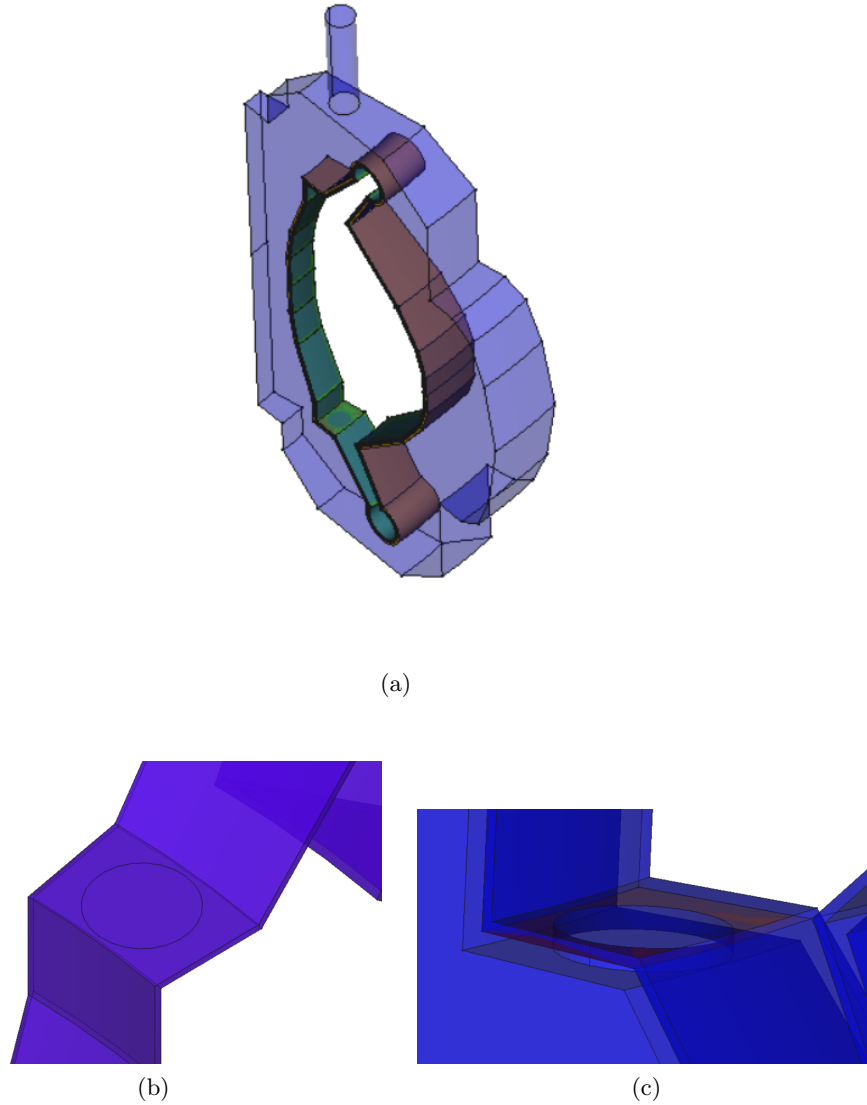


Figure 4.2: CAD produced in the framework of this work. Transparency regions correspond to the fluid domain. In figure only the FLiBe domain is shown, with a focus on the inlet patch (b) and on the connection port (c).

(TH) problem on two different meshes, with different characteristics, mapping then the computed fields from one mesh to the other using the OF utility *mapFields*. In particular, the NE mesh is coarser with respect to the TH one because the latter one has the boundary layers approaching the walls and a very refined zone in location of the connection port between the channel and the tank. It has been chosen to not perform

a classical grid independence analysis, which would have been too expensive from the computational cost, but use a different grid refinement approach based on the physics involved.

In particular, for what regards the TH mesh, the followed approach is based on the turbulent length scales. Since the k-epsilon turbulence model is been chosen, motivated by previous analysis [21], a turbulent length scale has been defined, following a dimensional analysis, as:

$$l_0 = \frac{k^{1.5}}{\varepsilon}. \quad (4.1)$$

That has been compared with the characteristic dimension of the cells (Δ), computed as

$$\Delta = V_{cell}^{1/3}, \quad (4.2)$$

where V_{cell} is the volume of the cell.

The two values must be compared, in order to understand if the produced mesh has been able or not to resolve effectively the turbulent phenomena. In particular, for RANS analysis, the suggested value for the l_0/Δ ratio is above 3 [36]. In figure 4.3 the map of the previously defined ratio is shown, limiting the range between the minimum computed value and the minimum acceptable value.

It is clear that the condition is satisfied in the majority of the fluid domain except of some locations in the channel.

The final mesh is shown in the 4.4, with a focus on the port of communication between the cooling channel and the tank, the transition from the first wall to the blanket and a comprehensive view of the lower part of the mesh, where the refinement is more appreciable. Regarding the colour subdivision of the different regions, green correspond to the first homogenized zone R1 (first wall and inner vacuum vessel), in red it is highlighted the fluid domain and in grey the second solid domain R2 (beryllium layer and outer vacuum vessel).

4.3 Neutronic setup

In analogy with the benchmark case, also for the blanket study, six energy groups have been chosen to represent the energetic distribution of the neutrons, with the same energy subdivision of table 3.1.

The nuclear properties and the thermal Doppler coefficients have been computed by means of the Monte Carlo Serpent code. Multiple probabilistic simulations have been conducted based on the very same geometry files presented in the previous section, at different temperatures. The imposed thermal range was the outcome of an initial complete OpenFOAM simulation, where no thermal feedback was allowed.

Regarding the boundary conditions, free surface BCs have been imposed on external patches of the blanket tank, interface BCs have been imposed on the internal patches of the different meshes and incoming current BCs have been imposed on the plasma facing patches.

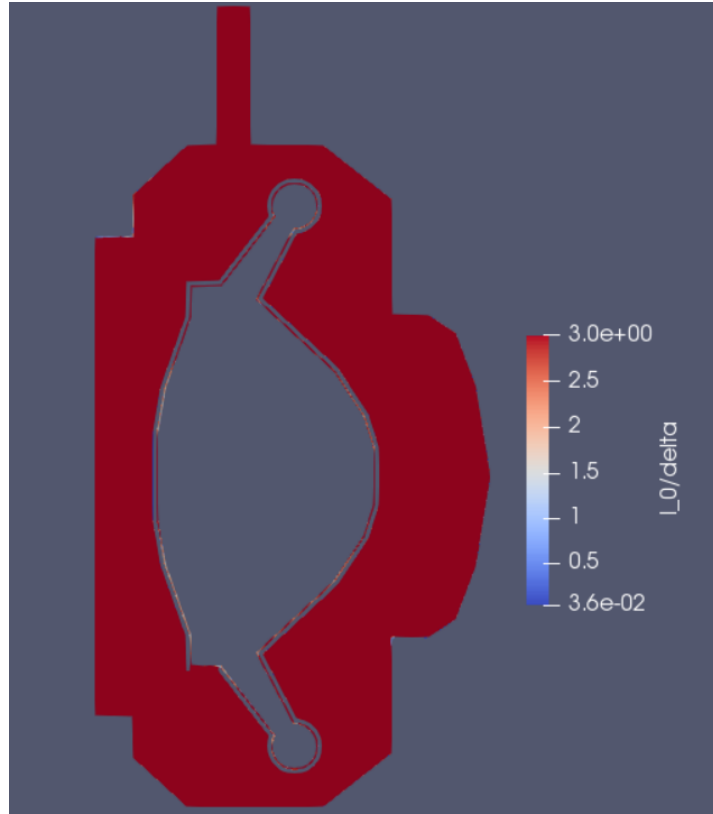


Figure 4.3: 2D map of the ratio l_0/Δ , the upper limit of the legend is set to the minimum allowed value (3) to facilitate the visualization of the bad cells.

Particular attention has been paid to the definition of the incoming neutron currents. Unluckily, in Serpent, the evaluation of neutron currents is very easy only when elemental shapes are used (torus, spheres...), but it is not trivial when the geometry is complex, that is the case of the ARC blanket. On the other hand, the evaluation of the fluxes is quite straightforward, requiring only the definition of a detector in a certain location of the domain. For these reasons, it has been chosen to compute the neutron currents on a toroidal surface of circular cross section limited to the central region of the plasma, and then, scale the obtained values by a factor equal to the ratio of the fluxes computed at the detector locations (generic position \vec{r}) and at the limit of the toroidal surface (\vec{r}_0):

$$J_{in}(\vec{r}) = J_{in}(\vec{r}_0) \cdot \frac{\Phi(\vec{r})}{\Phi(\vec{r}_0)}. \quad (4.3)$$

In the figure 4.8 it is shown the treatment of the incoming currents, highlighting with the same colour the patches on which the same current is imposed, please note that since the neutron source is symmetric with respect to the midplane, just half domain is reported.

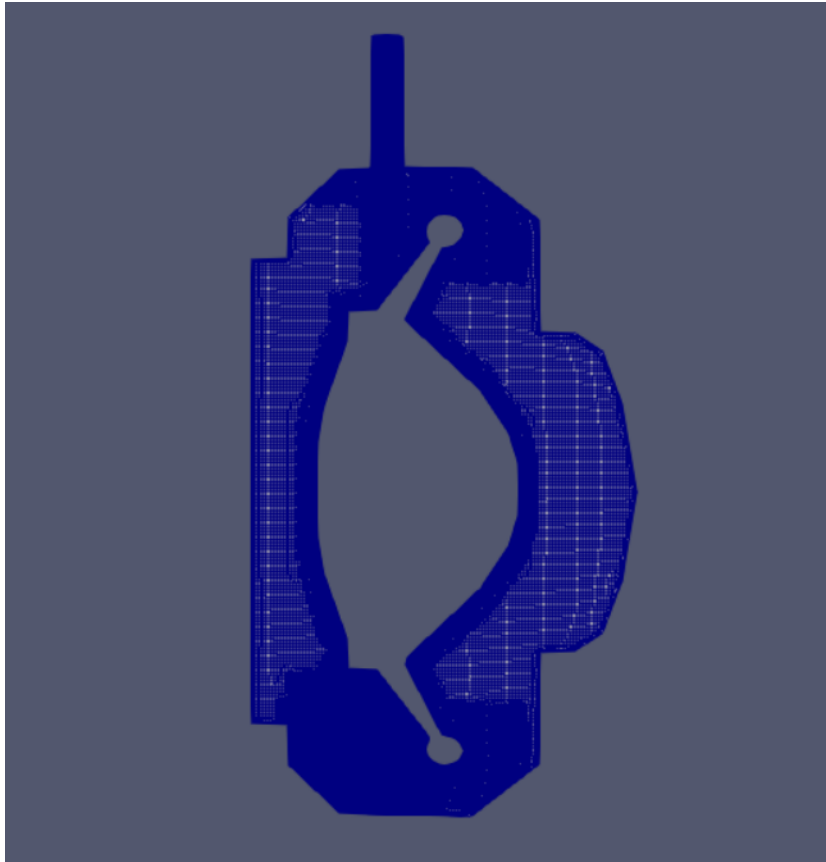


Figure 4.4: Thermal-hydraulics mesh - Complete view.

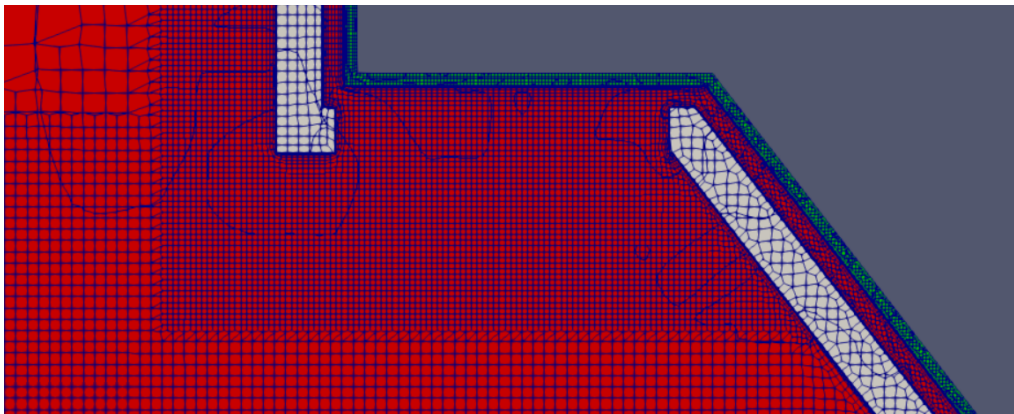


Figure 4.5: Thermal-hydraulics mesh - Focus on the connection port region.

4.4 Thermalhydraulic setup

The thermo-physical properties of the materials have been treated as temperature dependent. Particular attention has been made on the homogenized regions, in fact, it is

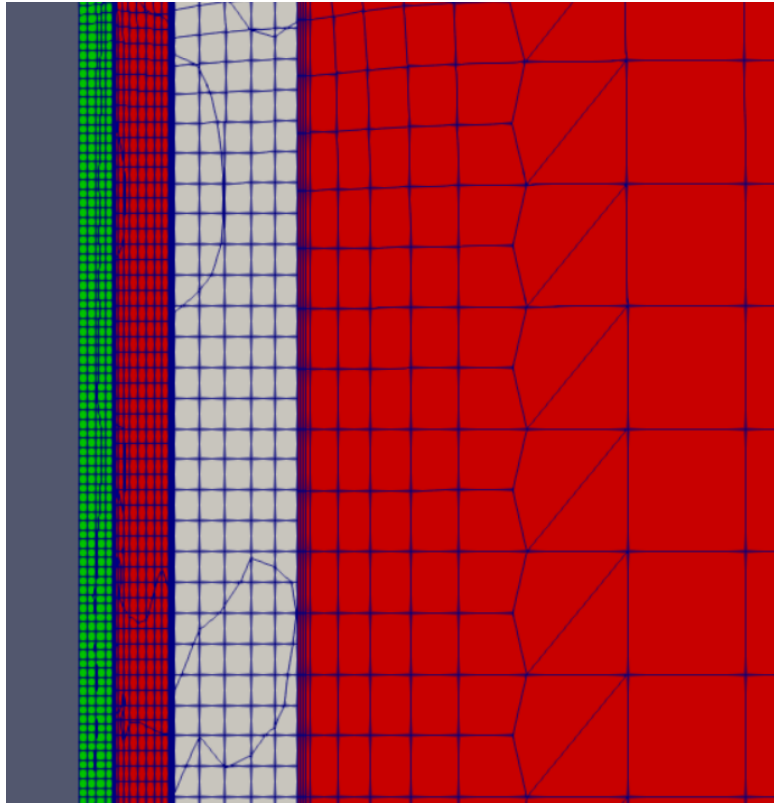


Figure 4.6: Thermal-hydraulics mesh - Focus on the transition of the dimension of the cells (green domain is R1, red domain is the FLiBe, white domain is R2).

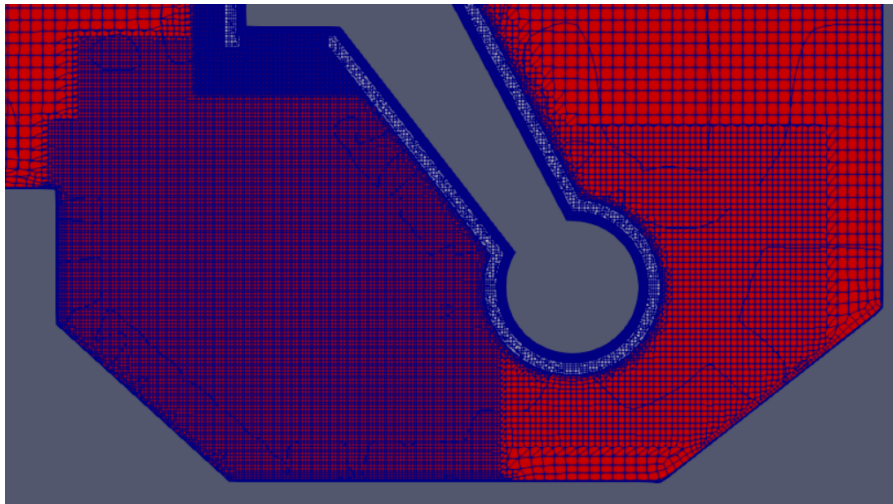


Figure 4.7: Thermal-hydraulics mesh - Focus on the lower blanket sector.

well known that when an homogenization is performed, the properties must be correctly

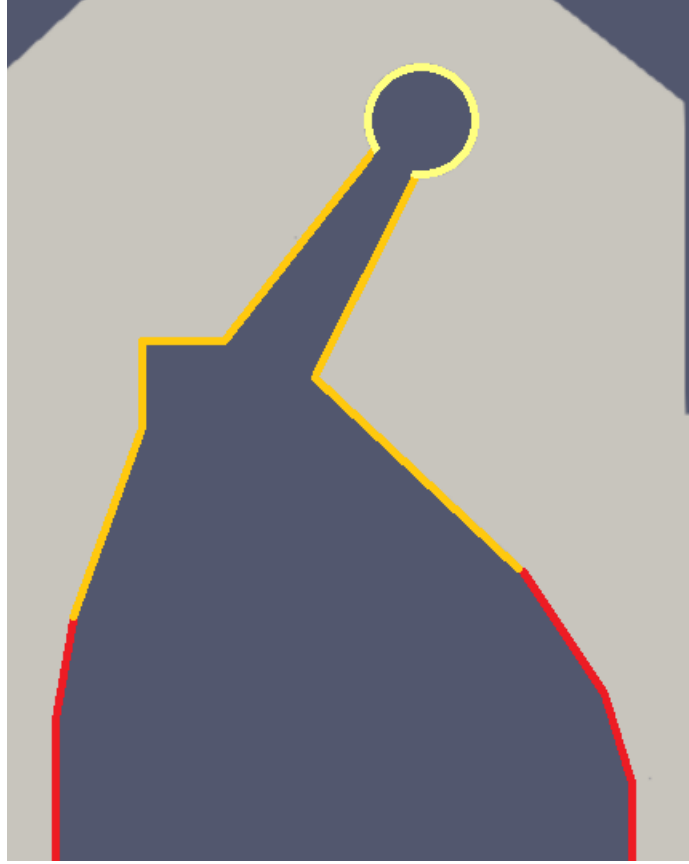


Figure 4.8: Characterization of the incoming neutron currents subdivision of the patches.

averaged on the volume (V) or on the mass (m) of the original materials. In particular, specific heat (c_p) must be averaged on the mass, while density (ρ) and thermal conductivity (k) on the volume:

$$c_{p_{hom}} = \sum_{i=1}^N \left(c_{p_i} \cdot \frac{m_i}{m_{tot}} \right), \quad (4.4)$$

$$\rho_{hom} = \sum_{i=1}^N \left(\rho_i \cdot \frac{V_i}{V_{tot}} \right), \quad (4.5)$$

$$k_{hom} = \sum_{i=1}^N \left(k_i \cdot \frac{V_i}{V_{tot}} \right), \quad (4.6)$$

For the homogenization process the volume values of table 4.1 have been used, and the correlations found in [37], [38] and [39] leading to the following functions:

$$c_{p_{R1}} = -1370 + 4.592 T - 3.657E - 03 T^2 + 9.665E - 07 T^3 \left[\frac{J}{kg \cdot K} \right], \quad (4.7)$$

$$\rho_{R1} = 9203 - 2.150E - 02 T - 2.029E - 06 T^2 + 7.735E - 19 T^3 \left[\frac{kg}{m^3} \right], \quad (4.8)$$

$$k_{R1} = 33.83 - 3.094E - 02 T + 3.965E - 05 T^2 - 1.206E - 08 T^3 \left[\frac{W}{m \cdot K} \right], \quad (4.9)$$

$$c_{pR2} = -1556 + 5.629 T - 4.480E - 03 T^2 + 1.196E - 06 T^3 \left[\frac{J}{kg \cdot K} \right], \quad (4.10)$$

$$\rho_{R2} = 6621 \left[\frac{kg}{m^3} \right], \quad (4.11)$$

$$k_{R2} = 79.53 - 1.269E - 01 T + 1.323E - 04 T^2 - 4.580E - 08 T^3 \left[\frac{W}{m \cdot K} \right]. \quad (4.12)$$

The properties of FLiBe are taken from [40], [41] and [42]:

$$c_{pFLiBe} = 2365 \left[\frac{J}{kg \cdot K} \right], \quad (4.13)$$

$$k_{FLiBe} = 0.6296 + 5E - 4 T \left[\frac{W}{m \cdot K} \right], \quad (4.14)$$

$$\mu_{FLiBe} = 0.4515 - 1.294E - 3 T + 1.271E - 06 T^2 - 4.227E - 10 T^3 [Pa \cdot s], \quad (4.15)$$

$$\rho_{FLiBe} = 2370 - 0.48 T + 2.0E - 05 T^2 \left[\frac{kg}{m^3} \right], \quad (4.16)$$

Regarding the boundary conditions for the fluid domain, the FLiBe is assumed to enter in the domain from the inlet patch with a velocity of 2.0 m/s and a fixed temperature of 800K; the outlet patch is set to be of the type *inletOutlet*, allowing outflow by means of the zero gradient condition, i.e. developed flow. This assumption has been made for two reasons: the first is that no information about the actual circuit is at the moment available, the second is that the outlet is not in the proximity of the exit of the tank, but it has been elongated voluntarily 1 meter far from it. The interface patches are been set as *turbulentTemperatureCoupledBaffleMixed* (ensuring the continuity of the heat flux and of the temperature profile) for the thermal treatment, while as walls for the hydraulic case. All the other patches (the external surface of the tank) are set to be adiabatic walls.

Regarding the solid domain, the interfaces are treated as the fluid ones, and the rest adiabatic, in order to ensure a conservative analysis.

The patches resulted by the cutting of the domain are set to be of the type *symmetry*.

4.5 Results

In this section are firstly presented the neutronic and power deposition results, than the flow field of the fluid domain, the temperature map of the blanket and the pressure distribution of FLiBe.

4.5.1 Power Deposition

The volumetric power deposition is the starting point of the thermal-hydraulic analysis, since it is fundamental that the cooling system is designed such that, at any time, it is able to extract the power deposited in the materials, both to guarantee both the structural integrity and efficient electricity production.

In the figure 4.9 is reported the final volumetric power deposition 2D map on a midplane section (remember that only neutrons are considered), where it is possible to see the effect of the non-uniform source, with practically a negligible amount of power deposited in the location of the divertors. The highest value of volumetric power is found in the cooling channel, with a peak value of $21 \text{ MW}/\text{m}^3$ occurring in the portions of the channel subjected to the maximum neutron fluence.

In the table 4.2 it is shown a comparison of the total power and the average volumetric power deposition calculated in this work and the result of a Monte Carlo Serpent simulation carried on the exact same geometry of this work.

Region	Power [MW]		Power density [MW/m ³]	
	nemoFoam	Serpent	nemoFoam	Serpent
Blanket	351	305	0.99	0.86
R1	15.9	14.6	4.44	4.09
R2	72.9	41.1	5.53	3.12

Table 4.2: Comparison of the power deposited and of the power density between the nemoFoam code and a Serpent simulation, carried out on the exact same geometry.

The computed values are clearly higher than the expected ones, with a maximum difference of the 78% in the case of the Region R2. The higher values of the volumetric power deposition can be addressed to the homogenization process performed in the solid materials. This hypothesis is motivated by the fact that the largest difference with the output of the probabilistic code is for the region R2, corresponding to the beryllium and vacuum vessel. The two materials have very different nuclear characteristics and since the aim of the former is to serve as neutron multiplier, role of relevant importance for the overall neutronic behaviour of the blanket, probably, the error introduced with this distortion of the real physics of the problem has been too big.

Taking into account the values of the average volumetric power and the volume of the produced CAD, the total power deposited (P_{tot}) in the blanket is evaluated, founding a value of 440 MW, between the reference value of 525 MW [7], which take into account also the power deposited by the photons, and the value of 370 MW computed in [20] and

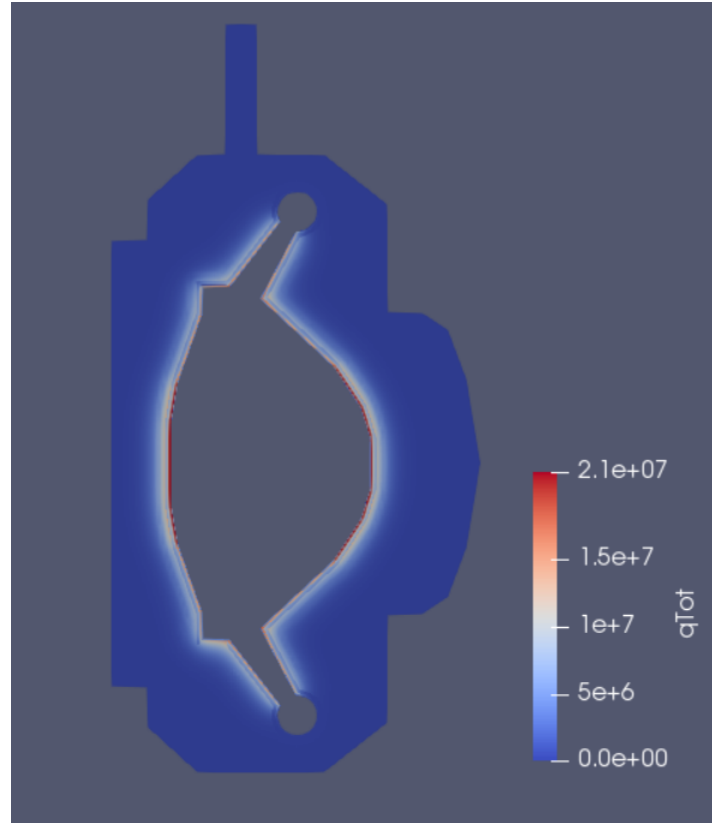


Figure 4.9: Volumetric power deposition 2D midplane map. The values are expressed in W/m^3 .

calculated through a Serpent simulation, corresponding to the power deposited only by the neutrons.

It is important to analyze the spatial power profile in order to obtain detailed information on how power is actually deposited in the materials. Global average values, being weighted (with the same importance) on regions where the neutron flux is very low (divertors) and where is at its maximum (equatorial plane), do not allow to understand where hot spots can occur, leading, for example, to possible local failure of the structural materials. From figure 4.10, where the power trend is extracted on an horizontal line passing through the centre of simmetry of the blanket, and from figure 4.11, where the same operation is performed along a line perpendicular to the upper divertor legs, it is clear that the maximum values of the volumetric power are well beyond the average values of the table 4.2 for all the materials. Temperature peaks are foreseen in the equatorial region on the surfaces in contact with region R2.

4.5.2 Flow field

Restricting the analysis on the fluid domain, it is possible to analyze the flow field of the FLiBe in the blanket tank and in the coolant channel, shown comprehensively in figure

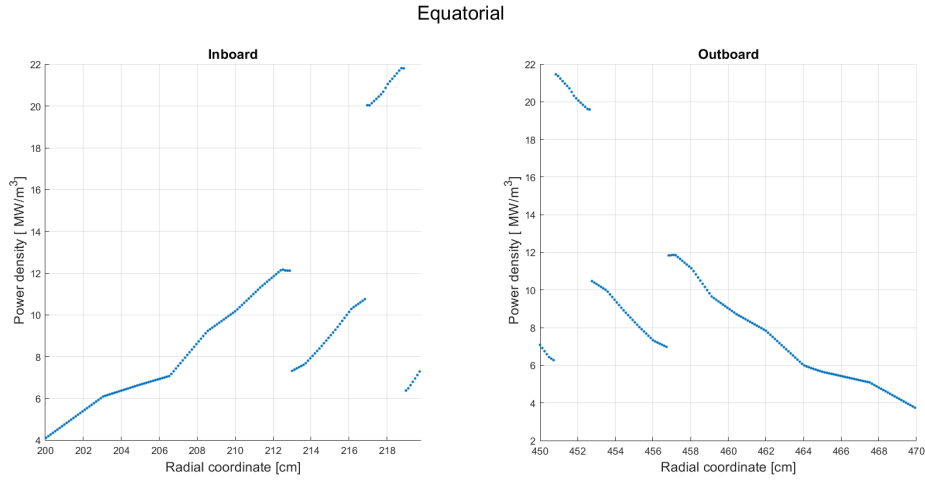


Figure 4.10: Volumetric power deposition profiles at the equatorial plane section.

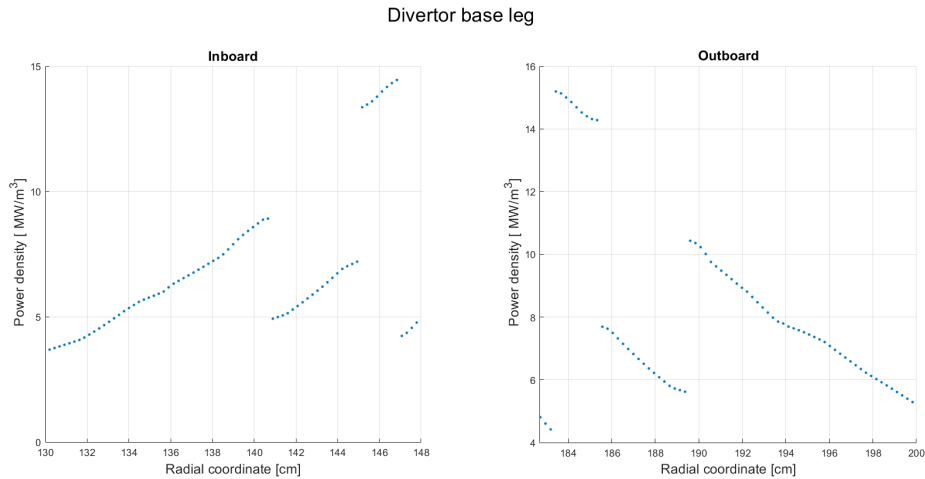


Figure 4.11: Volumetric power deposition profiles at the base of the legs of the divertors.

4.12. The cross section area of the channel is, clearly, orders of magnitude smaller than in the tank, but also with respect to the inlet patch (although the difference is smaller), for this reason, given the inlet velocity of 2.0 m/s , the maximum value reached in the channel is of 15 m/s . The flow, here, is highly turbulent, ensuring good heat removal capabilities from the surrounding solid materials.

Downstream the connection port with the tank, thanks to the abrupt variation of cross section area, the flow spreads rapidly approaching a kind of jet-type flow, with a consequent lowering of the velocity, that characterize the flow field in the whole blanket

tank.

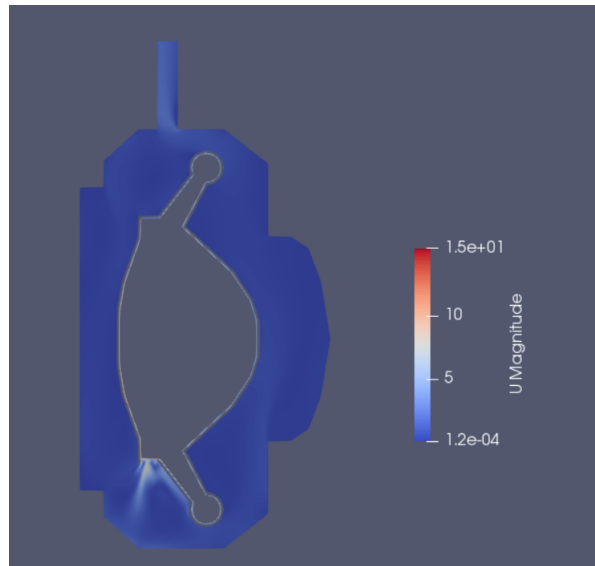


Figure 4.12: 2D map of the magnitude of the velocity in the fluid domain. Values are expressed in [m/s].

The inlet flow rate imposed on the corresponding patch is 279.69 kg/s , while the computed one at the outlet patch is of 279.84 kg/s , with a relative error of 0.05% , ensuring mass continuity.

Focusing on the coolant channel, after the inlet, the flow bifurcates into two streams, that have been found to have comparable mass flow rates. This fact is of particular interest, since it seems that the combined effects of the different cross section flow areas and of the localized losses in correspondence of the elbows produce the same global hydraulic resistance, across, in principle, two very different pathways. The velocity of the FLiBe in the inner and in the outer branches of the coolant channel depends mainly on the cross section flow area of the channel that in its turn depends on the distance from the rotation axis of the torus. In the figure 4.13, where a section of the coolant channel is performed with a plane of normal $(0,0,1)$, this behaviour is clearly appreciable. In figure 4.14, are reported the profiles of the velocity, both at the inboard and outboard pathways.

Particular attention must be paid to the elbows, since in that occurrence the flow is forced to change direction, i.e. accelerates, producing a variation of the flow field, in fact: if a portion of the fluid increases its velocity, another one has to decrease it. The effect of this phenomena is the possibility that low velocity regions (typically the corner opposite to the direction of the elbow) can become hot spots, while high velocity locations can become critical point from the corrosion point of view. The following figures report a focus on the upper divertor region and of the elbow on the outboard pathway just before the divertor leg.

The flow field in the blankt tank, instead, is characterized by low velocities, leading to worse heat transfer capabilities that are compensated by the fact that the volumetric

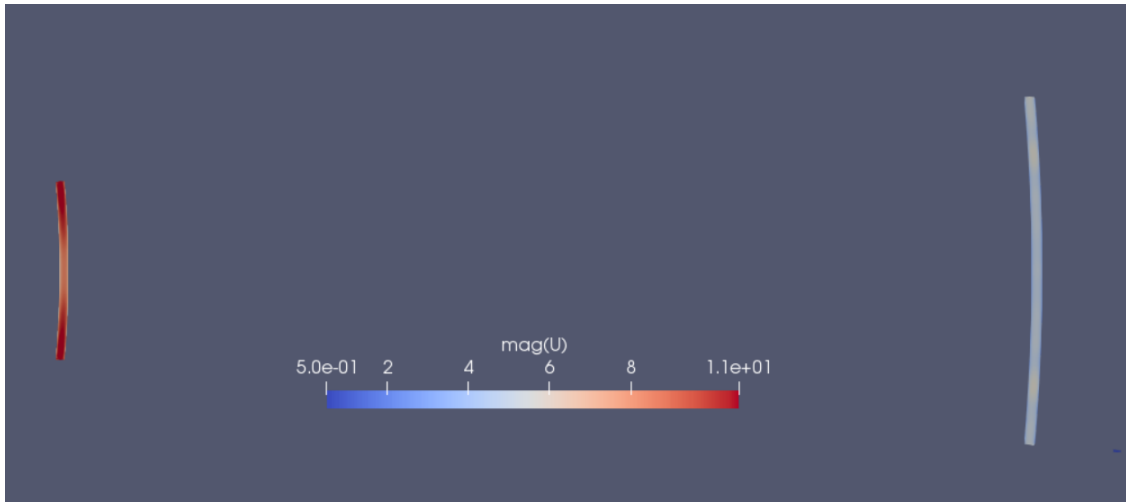


Figure 4.13: Comparison of the flow field in a midplane section of the coolant channel. Values are expressed in [m/s].

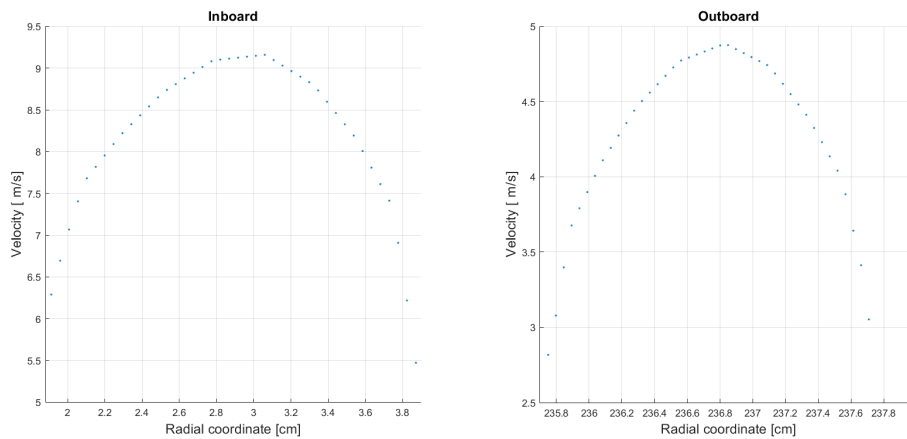


Figure 4.14: Average velocity profile on the same midplane section of the coolant channel of fig. 4.13.

power deposition, as shown by figure 4.10 and 4.11, is one order of magnitude smaller than in the channel, already after 20 cm from the Inconel718 surface. Regions of relatively higher velocities are the restrictions that occur in proximity of the divertors and near the outlet pipe, as figure 4.16 shows.

The FLiBe exiting from the port, starts to move upwardly, in particular it bifurcates into two streams, one going through the outboard region and one through the inboard. The region after the port, there the fluid expands, present a complex structure that will require additional attention in future works, adopting, probably, a specific turbulence

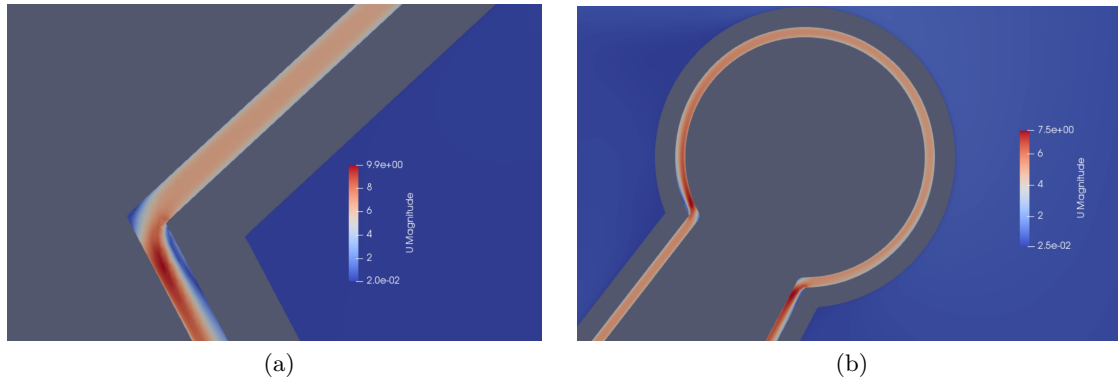


Figure 4.15: Flow fields in the upper divertor sector of the coolant channel. Values are expressed in [m/s].

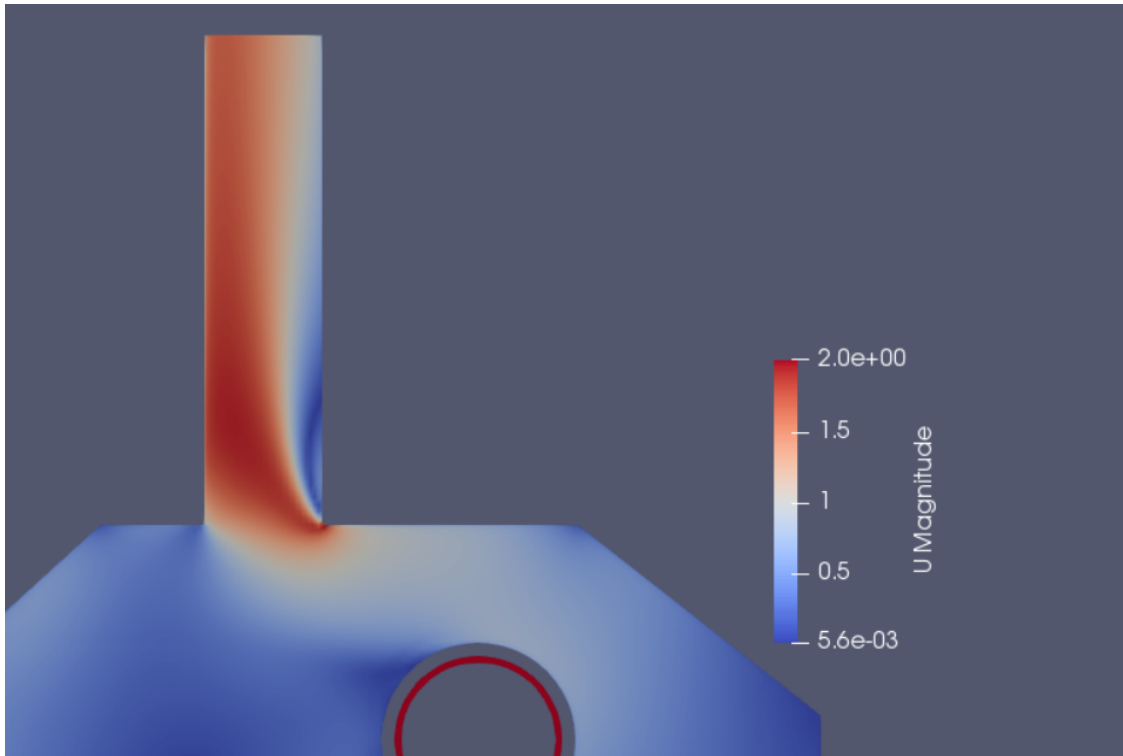


Figure 4.16: Flow fields upper sector of the blanket tank. Values are expressed in [m/s].

model suited for high Prandtl number fluids (FLiBe belongs to this category of fluids). The effectiveness of the turbulence model influences the presence and the development of the recirculation regions too, characterized by the circular motion of the fluid, where the higher blanket hotspots are expected.

Some recirculation regions develop both in the inboard sector and in the outboard,

as shown in figure 4.17. In particular, the ones in the external segment are characterized by a wider radius and lower velocity, possibly the most subjected to become hotspots.

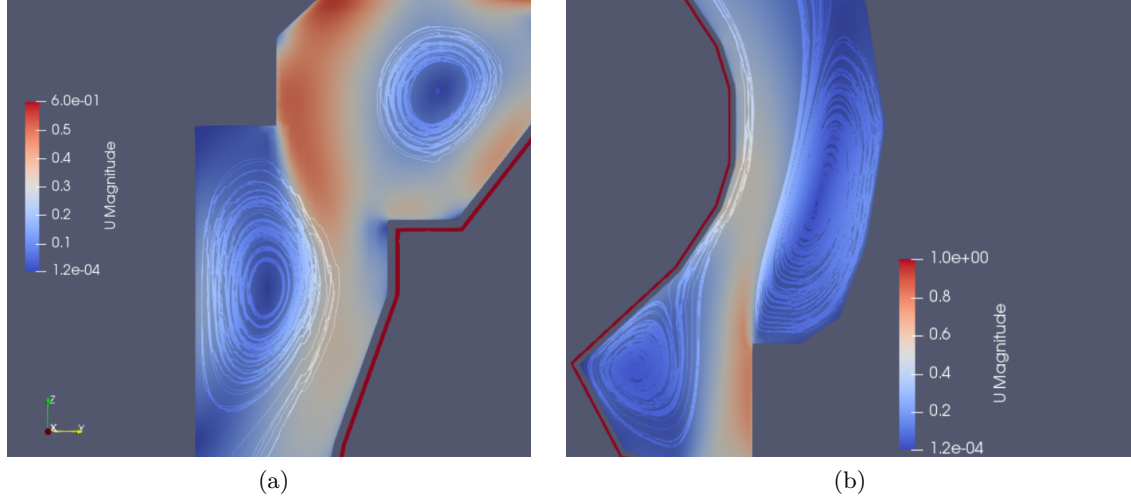


Figure 4.17: Recirculation patterns in the inboard and in the outboard sector of the blanket tank. Values are expressed in [m/s].

4.5.3 Temperature map

The temperature distribution depends on the volumetric power deposition, on the flow field, on the geometry and on the thermo-physical properties of the materials. Figure 4.18 shows the map of the temperature, on the usual 2D midplane section, where it is possible to see the combined effect of the previous drivers. It is evident that, thermally, the blanket can be subdivided into two halves: the inboard region that is characterized by higher temperatures, especially in proximity of the patches where the incoming neutron current has been set to the maximum value, and by a smaller flow rate; the outboard region, instead, presents lower temperatures, despite of the presence of the biggest recirculation zone (fig. 4.17), mainly thanks to the higher mass flow rate (236.5 kg/s) and to the relative higher thermal capacity of the region.

The outlet average temperature (T_{out}) of the FLiBe is found to be 818.7 K, which correspond to a slightly higher temperature increase (2.3%), respect to the the computed one from the theoretical power balance in the FLiBe domain:

$$P_{tot} = \dot{m} c_p \Delta T = \dot{m} c_p (T_{out} - T_{in}), \quad (4.17)$$

where P_{tot} is the sum of the power deposited in the solid and in fluid regions. It turns out that the FLiBe exits from the coolant channel with an average temperature of 807.5 K, then it reaches its maximum temperature in the inboard region, and finally, thanks to the mixing (before the outlet pipe) with the cold fluid coming from the outboard section, exits with the found value. The evaluated average temperatures of the FLiBe both at the

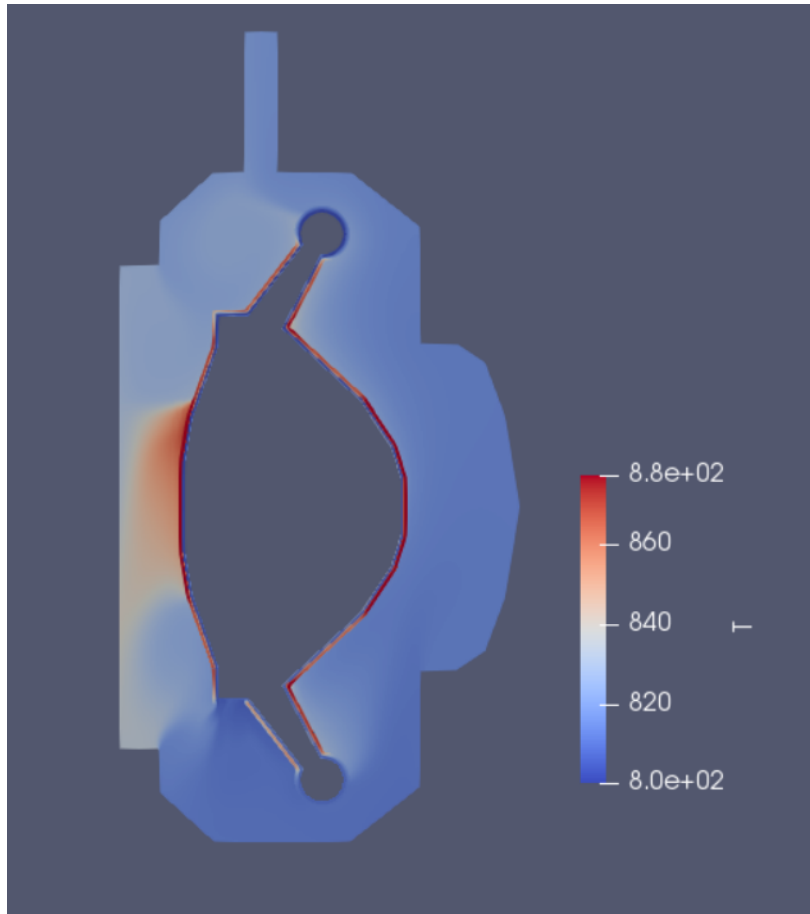


Figure 4.18: Temperature map of the blanket, solid layers are included. Values are expressed in [K].

port and the outlet permit to compute which is the fraction of the total power extracted from the fluid in the coolant channel and in the blanket tank. In particular, the 40% of the total power is extracted in the first sector, while the remaining part in the blanket.

Focusing on the temperature map of the coolant channel, shown in the figure 4.19, it is found that the inboard flow experiences a lower temperature gain with respect to the outboard one. In the flow field section, it has been shown that after the inlet the FLiBe splits in two streams of comparable flow rate, therefore, since for the same flow rate, the higher increase in temperature occur in the one which receives more energy, this must be the case of the outboard flow. The longer distance covered with a lower velocity make the FLiBe flowing in the outboard sector to stay more time in the channel, increasing the total amount of energy received. For this reason the hot spot of the coolant channel occurs in proximity of the last elbow, before the port, on the outboard segment.

Focusing on the temperature distribution in the solid layers, showed in the figure 4.20, it is found that the region R2 is the hottest one, with a peak temperature of 920 K, compliant with the thermal limits of the Inconel718. The computed value is, however,

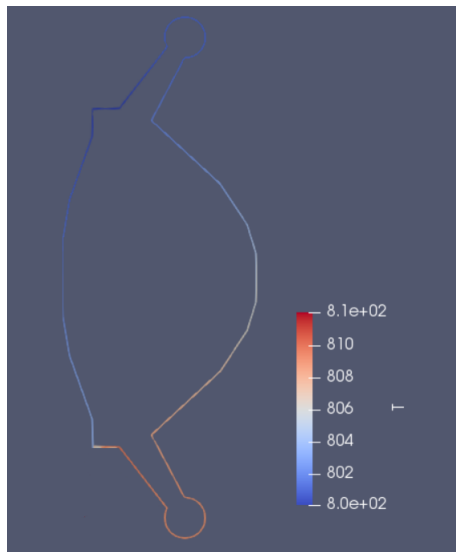


Figure 4.19: Temperature map of the coolant channel. Values are expressed in [K].

obtained on an homogenized system, therefore, future analysis should implement each region by itself to discover if the thermal requirements are actually satisfied or not.

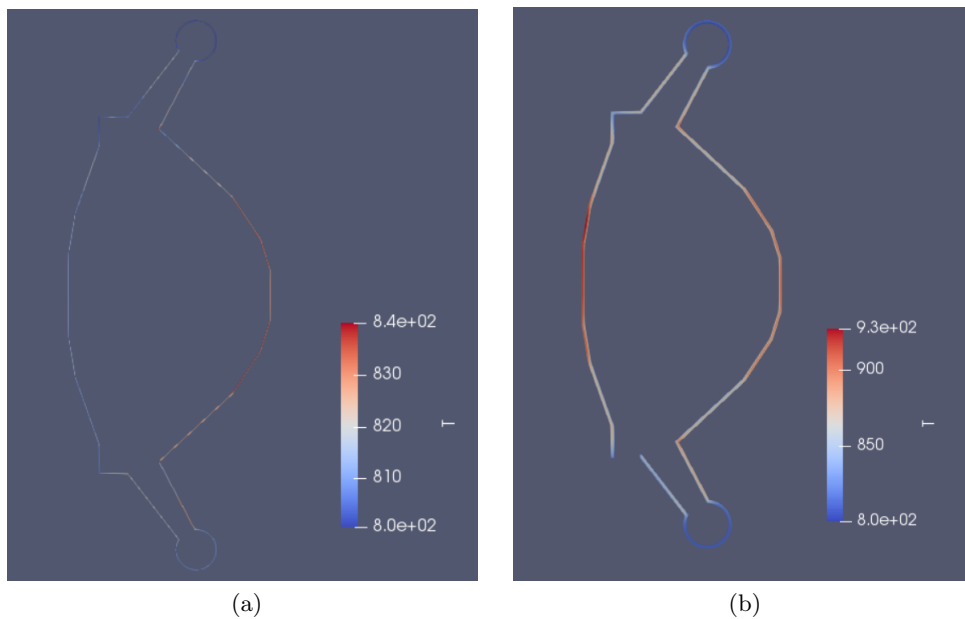


Figure 4.20: Temperature map of the R1 domain (a) and of the R2 domain (b). Values are expressed in [K].

4.5.4 Pressure field

The computed pressure field for the Blanket is obtained by imposing an outlet pressure of 0 Pa (gauge). The main player in the pressure variation in the tank, thanks to the large cross section areas and the few elbows, is gravity.

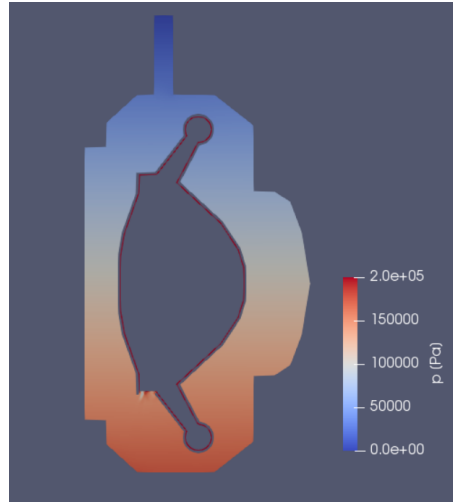


Figure 4.20: Pressure field of the fluid domain.

In the channel, instead, the high velocities of the fluid and the sharp variations of direction, produce additional pressure losses, such as figure 4.21 shows. Across the divertors section of the channel (from one leg to the other) there is an important pressure drop in the order of 0.8 bar.

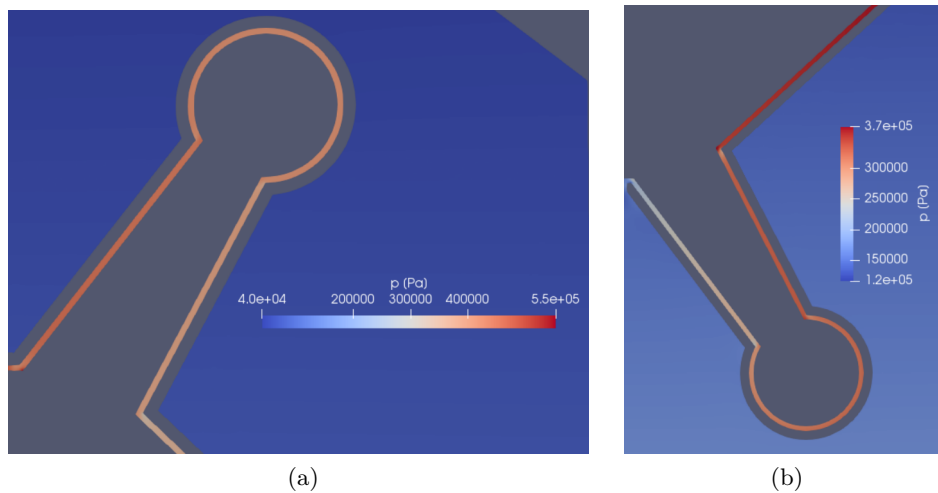


Figure 4.21: Pressure field across the divertor sectors.

Chapter 5

Conclusion

In the framework of this thesis, a finite volume tool has been developed in the OpenFOAM environment and used to model the steady state of the blanket of the ARC reactor. A multi-physics analysis has been conducted, coupling bidirectionally the neutronic and the thermal-hydraulics behaviours. Taking into account the reciprocal effect of each physical problem is mandatory to obtain solid results in similar problems.

The flow and the pressure fields have been computed for the FLiBe domain, while the temperature map and the volumetric power distribution have been calculated for both the fluid and the solid regions.

With the used setup, very high velocities have been found in the coolant channel, leading to possible corrosion issues, but showing effective heat extraction performance; no temperature limit has been overcome and a total pressure drop of about 5 bar has been computed.

The conducted 3D analysis relied on an unstructured mesh that showed the capability of resolving the turbulent length scales (associated to the $k - \varepsilon$ turbulence model) in the quasi totality of the domain.

Some approximations have been performed, mainly on the geometry, since a simplified version of the hydraulic layout has been investigated and the solid regions have been properly homogenized to reduce the number of cells and allow the calculations to be performed in a couple of days.

The presented model can serve as starting base for further, refined analysis which should take into account the actual geometries of the blanket; the effects of Magnetohydrodynamics (MHD) on the flow field and on the heat transfer processes; the possible impact of radiative heat transfer (due to the high temperatures foreseen); the impact of the chemical reactions of Lithium (both exothermic and endothermic) occurring in the blanket and the integration of photons propagation in the module of power deposition. Time dependent models can be an additional further step in the development of the model.

The finite volume approach has shown promising capabilities in the framework of the multi-physics analysis, thanks to its flexibility and the capability of solving very different physical problems in the same tool.

Bibliography

- [1] IEA, *Electricity Market Report - July 2021*, Paris <https://www.iea.org/reports/electricity-market-report-july-2021>, (2021).
- [2] IEA, *Electricity Market Report - July 2022*, IEA, Paris <https://www.iea.org/reports/electricity-market-report-july-2022>, (2022).
- [3] Marta M. Gospodarczyk, *IAEA Department of Nuclear Energy, Amid Global Crises, Nuclear Power Provides Energy Security with Increased Electricity Generation in 2021*, (2021), accessed 4 October 2022, <<https://www.iaea.org/newscenter/news/amid-global-crises-nuclear-power-provides-energy-security-with-increased-electricity-generation-in-2021>>
- [4] Hunyadi Murph, Simona E. and Murph, Melissa A., "*Nuclear fusion: the promise of endless energy*", Physical Sciences Reviews, (2022).
- [5] J. P. Freidberg, "*Plasma Physics and Fusion Energy*", Cambridge University Press, (2007).
- [6] Hesch, K. Boccaccini, L.V. Stieglitz, Robert., "*Blankets – key element of a fusion reactor – functions, design and present state of development.*", Kerntechnik, 83, (241-250), (2018).
- [7] B.N. Sorbom, J. Ball, T.R. Palmer, F.J. Mangiarotti, J.M. Sierchio, P. Bonoli, C. Kasten, D.A. Sutherland, H.S. Barnard, C.B. Haakonsen, J. Goh, C. Sung, D.G. Whyte, "*ARC: A compact, high-field, fusion nuclear science facility and demonstration power plant with demountable magnets.*", Fusion Engineering and Design, 100, (378-405), (2015).
- [8] G. Federici et al., "*DEMO design activity in Europe: Progress and updates.*", , Fusion Engineering and Design, 136-A, (729-741), (2018).
- [9] Farrokh Najmabadi et al., "*The ARIES-AT advanced tokamak, Advanced technology fusion power plant.*", , Fusion Engineering and Design, 80, (3-23), (2006).
- [10] Jha Alok K., Matsumoto Kaname, "*Superconductive REBCO Thin Films and Their Nanocomposites: The Role of Rare-Earth Oxides in Promoting Sustainable Energy.*", Frontiers in Physics, 7, (2019).
- [11] Igochine, Valentin, "*Investigation of MHD instabilities in conventional and advanced tokamak scenarios on ASDEX upgrade.*", Elektronische Ressource, (2022).
- [12] Commonwealth Fusion Systems, "*ARC: Commercialization.*", <https://cfs.energy/technology/arc-commercialization>.
- [13] F. Carotti, M. Abou Dbai, K. Ahmed, R. O. Scarlat, "*Experimental and modeling studies of over-cooling transients in fluoride-salt cooled high-temperature reactors.*", NURETH-16, (2015).

-
- [14] Weller, H.G. Tabor, Gavin Jasak, Hrvoje Fureby, Christer, "A Tensorial Approach to Computational Continuum Mechanics Using Object Orientated Techniques.", *Computers in Physics*, (12), 620-631, (1998).
- [15] The Architects of OpenFOAM, *About OpenFOAM*, <<https://cfd.direct/openfoam/about/>>, accessed 4 October (2022).
- [16] Wendell Horton, Sadruddin Benkadda, *ITER Physics*, World Scientific Publishing, (2015).
- [17] M.R. Gordinier, J.W. Davis, F.R. Scott, K.R. Schultz, *Encyclopedia of Physical Science and Technology (Third Edition)*, Nuclear Fusion Power, 671-699, (2003).
- [18] <https://cfe.ukaea.uk/research/joint-european-torus/>
- [19] SpecialMetals, *INCONEL® alloy 718*, Special Metals Corporation, (2007).
- [20] Alex Aimetta, Nicolò Abrate, Sandra Dulla, Antonio Froio, *Neutronic Analysis of the Fusion Reactor ARC: Monte Carlo Simulations with the Serpent Code*, Fusion Science and technology, (2022).
- [21] A. Sircar, J. W. Bae, E. Peterson, J. Solberg, V. Badalasi, *FERMI: A multi-physics simulation environment for fusion reactor blanket*, NURETH-19, (2022).
- [22] A.Q. Kuang et al., *Conceptual design study for heat exhaust management in the ARC fusion pilot plant*, Fusion Engineering and Design, 137, 221–242, (2018).
- [23] John R. Lamarsh, *Introduction to nuclear reactor theory*, New York University, (1961).
- [24] Bell, G. I., and Glasstone, S, *Nuclear Reactor Theory*, US Atomic Energy Commission, (1970).
- [25] Munson Bruce R. et al., *Fundamental of fluid mechanics*, John Wiley Sons, Inc., (2013).
- [26] Incropera Frank P., *Introduction to heat transfer*, John Wiley Sons, Inc., (2011).
- [27] Moukalled F. et al., *The Finite Volume Method in Computational Fluid Dynamics*, Springer, (2015).
- [28] H K Versteeg and W Malalasekera, *An Introduction to Computational Fluid Dynamics*, Pearson Education, (2007).
- [29] Christopher J. Greenshields, *OpenFOAM User Guide - version 10*, (2022).
- [30] Manuele Aufiero et al., *Development of an OpenFOAM model for the Molten Salt Fast Reactor transient analysis*, (2013).
- [31] <https://github.com/NEMO-Group/nemoFoam>
- [32] Leppänen, J., et al., "The Serpent Monte Carlo code: Status, development and applications in 2013.", *Ann. Nucl. Energy*, 82, 142-150, (2015).
- [33] <https://www.freecadweb.org>
- [34] <https://www.salome-platform.org/>
- [35] <https://github.com/wyldckat/cfMesh>
- [36] Guerrero - wolfdynamics, "Advanced meshing using OpenFOAM technology: blockMesh and snappyHexMesh", Online Training Advanced session, (2022).
- [37] P. Tolias, "Analytical expressions for thermophysical properties of solid and liquid tungsten relevant for fusion applications.", *Nuclear Materials and Energy*, 13, 42-57, (2017).

- [38] P. Tolias, "*Analytical expressions for thermophysical properties of solid and liquid beryllium relevant for fusion applications.*", Nuclear Materials and Energy, 31, (2017).
- [39] A Sh Agazhanov et al., "*Thermophysical properties of Inconel 718 alloy.*", Journal of Physics, (2019).
- [40] T. Lichtenstein et al., "*Thermochemical Property Measurements of FLiNaK and FLiBe in FY 2020.*", Argonne National Laboratory, (2020).
- [41] Manohar S. Sohal et al., "*Engineering Database of Liquid Salt Thermophysical and Thermochemical Properties.*", Idaho National Laboratory, (2013).
- [42] Paul W. Humrickhouse and Brad J. Merrill, "*Revised Equation of State for FLiBe in MELCOR.*", Idaho National Laboratory, (2017).